Valleytronic full configuration-interaction approach: Application to the excitation spectra of Si double-dot qubits

Constantine Yannouleas and Uzi Landman

Phys. Rev. B **106**, 195306 — Published 23 November 2022

DOI: 10.1103/PhysRevB.106.195306

Valleytronic full configuration-interaction approach: An application to the excitation spectra of Si double-dot qubits

Constantine Yannouleas* and Uzi Landman†
School of Physics, Georgia Institute of Technology, Atlanta, Georgia 30332-0430

(Dated: 9 November 2022)

A study of the influence of strong electron-electron interactions and Wigner-molecule (WM) formation on the spectra of $2e$ singlet-triplet double-dot Si qubits is presented based on a full configuration interaction (FCI) approach that incorporates the valley degree of freedom (VDOF) in the context of the continuous (effective mass) description of semiconductor materials. Our FCI solutions correspond to treating the VDOF as an isospin in addition to the regular spin. A major advantage of our treatment is its capability to assign to each energy curve in the qubit's spectrum a complete set of good quantum numbers for both the spin and the valley isospin. This allows for the interpretation of the Si double-dot spectra according to an underlying $\mathrm{SU}(4) \supset \mathrm{SU}(2) \times \mathrm{SU}(2)$ group-chain organization. Considering parameters in the range of actual experimental situations, we demonstrate for the first time in a double-dot qubit that, in the (2,0) charge configuration and compared to the expected large, and dot-size determined, single-particle (orbital) energy gap, the strong $e-e$ interactions drastically quench the spin-singlet−spin-triplet energy gap, $E_{\rm ST}^{\oplus}$, within the same valley, making it competitive to the small energy gap, E_V, between the two valleys. We present results for both the $E_{\rm ST}^{\oplus} < E_V$ and $E_{\rm ST}^{\oplus} > E_V$ cases, which have been reported to occur in different experimental qubit devices. In particular, we investigate the spectra as a function of detuning and demonstrate the strengthening of the all-important avoided crossings due to a lowering of the interdot barrier and/or the influence of valley-orbit coupling. We further demonstrate, as a function of an applied magnetic field, the emergence of avoided crossings in the (1,1) charge configuration due to the more general spin-valley coupling, in agreement with experiments. The valleytronic FCI method formulated and implemented in this paper, and demonstrated for the case of two electrons confined in a tunable double quantum dot, offers also a most effective tool for analyzing the spectra of Si qubits with more than two wells and/or more than two electrons, in field-free conditions, as well as under the influence of an applied magnetic field. Furthermore, it can also be straightforwardly extended to the case of bilayer graphene quantum dots.

I. INTRODUCTION

Studies of semiconductor qubits (e.g., Si [1–7] and GaAs [8–10] electron-based qubits, or Si [11, 12] and Ge [13–17] hole-based ones) are developing into major research endeavors, with each material and charge carrier type presenting its own opportunities and/or challenges. In this paper, we focus on electron-based Si double-quantum-dot (DQD) qubits, which are of high interest due to their inherent long coherence times [1–4].

For Si qubits, the challenge consists of the presence of the valley degree of freedom (VDOF); namely, the VDOF brings along added complexity (compared to cases where the VDOF is absent, e.g., GaAs nanodevices [8, 9, 18]), which has been addressed in a number of experimental and theoretical treatments [1, 19–30]. Indeed, a number of publications consider this complexity as a challenge to be overcome or to do away with (see, e.g., Refs. [1, 20, 22, 27]), whereas a second group of publications (see, e.g., Refs. [23, 25, 28–30]) considers it as a potential resource to be further explored. Experimental efforts in both directions are intensely pursued, but a definitive resolution has not been reached as yet.

Further progress toward understanding of the VDOF complexity in solid-state qubits is compounded by the very recent realization (i.e., in 2021) that the energy gaps in the relevant excitation spectra (with the potential to be involved in the operation of the qubit) depend crucially [12, 29, 31–33] on Wigner-molecule (WM) [18, 34–45] formation and the strong electron-electron interactions that naturally arise in these silicon nanodevices (also found in GaAs 3e hybrid qubits [9, 46, 47]), due to an interplay between materials parameters, as well as size and geometry (e.g., circular or wire-like shapes of the QDs), that yields large values for the Wigner parameter $R_W > 1$; see Sec. II A. We note that the concept of Wigner molecules originated from theoretical investigations more than two decades ago (see Refs. [34, 35], and Ref. [44] for a Review). We further note that, due to its very nature, Wigner-molecule formation is universal and of relevance to many other condensed-matter and atomic-and-molecular physics situations, like trapped few-particles under an applied magnetic field or strong rotations, whether fermions (electrons or fermionic ultracold neutral atoms) or bosons (bosonic ultracold atoms); see, e.g., Refs. [44, 48–53].

The present paper focusses primarily on deciphering the complexity of the excitation spectra in the case of a Si DQD qubit in the physically relevant regime of strong $e-e$ interactions and WM formation. These strongly-

---

* Constantine.Yannouleas@physics.gatech.edu
† Uzi.Landman@physics.gatech.edu

correlated spectra will be shown to be multifaceted compared to those investigated recently for the case of a single Si QD [12, 29, 31–33], due to the additional degrees of freedom associated with the detuning, the separation, and the variable barrier between the QDs.

Among the various many-body approaches employed in this area of research, it is becoming increasingly transparent that the strong $e-e$ interaction regime in few-electron nanosystems (and in particular, the elucidation of the effects of WM formation in both the ground and excited states) can be most accurately described theoretically through the use of the microscopic full configuration interaction (FCI) methodology [54], which treats in an efficient manner the two-body part of the Hamiltonian governing the system. Indeed, the FCI (referred to also as exact diagonalization) has been successfully applied [18, 41–43, 45–48] in the last two decades to two-dimensional (2D) quantum dots (QDs) with single-band semiconductor materials substrates, like GaAs. FCI calculations for condensed-matter nanostructures that incorporate aspects of the VDOF have been also considered recently [32, 55]. However, a CI approach that unequivocally relates to the field of valleytronics [56–60] by properly incorporating the valley degree of freedom as an isospin [61], in complete analogy with the regular spin, is still missing.

Here, we fill this gap by introducing a valleytronic FCI (VFCI) approach that employs single-particle (one-body) bases associated with the continuum-model (effective mass approximation [62] of the two-band structure in Si QDs [63]). The VFCI methodology developed and implemented in this work, as well as the one-band FCI employed in Refs. [46, 47], represent a significant step towards gaining a comprehensive understanding of the complexity of the spectra of semi-conductor-based solid state qubits. These methodologies enable accurate many-body computational modeling of quantum dot devices (coupled quantum dots of variable sizes, and shapes, ranging from two-dimensional circular ones, to elliptical and wire-like quasi-one-dimensional structures), with (this paper) or without [46, 47] valeytronic characteristics, allowing for formation of carrier-localized correlated-structures (i.e, WMs [18, 34–45]).

The utilization and merits of the VFCI methodology presented in this paper are demonstrated through its application for a comprehensive exploration of the properties of the valleytronic spectra of a pair of electrons in a Si double-quantum-dot, including changes brought about by detuning between the two potential wells, with and without the application of an external magnetic field. The main achievements of our explorations may be summarized as: (i) Complete description of the valley degree of freedom with adaptation of the isospin concept, in full analogy with the regular spin; (ii) Uncovering the group theoretical $\mathrm{SU}(4) \supset \mathrm{SU}(2) \times \mathrm{SU}(2)$ spectral organization, with the emergence of avoided-crossings and the dependence on spin-isospin coupling strength; (iii) Demonstration of the formation of WMs, driven by strong $e-e$ correlations, occurring for experimentally–relevant double-well confinements, with the consequent appearance of strongly suppressed spin-singlet/spin-triplet gaps within the same valley, thus affecting the operational gating-characteristics of the quantum double-dot; (iv) Analysis of the influence of valley-orbit and spin-valley Hamiltonian terms, in particular under an applied magnetic field. In light of the above, it is foreseen, that the valleytronic FCI method demonstrated here, will be found to be most valuable for future investigations, particularly, for in-depth understanding of the spectra of Si (as well as other semiconductors, e.g. Ge) qubits with multiple wells, and geometries, including spherical, elliptical, and wire-like quasi-one-dimensional structures.

We stress that the VFCI methodology introduced here enables the acquisition of numerical results complete with full spin-isospin assignments that reveal the underlying $\mathrm{SU}(4) \supset \mathrm{SU}(2) \times \mathrm{SU}(2)$ [64–66] group-chain organization of the spectra of Si double-quantum-dot (DQD) qubits. Specifically, the valley isospin assignments in our VFCI consist of a pair of indices $(\mathcal{V}, V_z)$ in analogy with the two indices $(\mathcal{S}, S_z)$ of the regular spin. (This is in contrast with earlier CI implementations in single QDs constructed from other materials exhibiting a VDOF, which have been restricted [67] to characterizing the CI states using one valley index only, namely the valley projection V_z [68].)

Furthermore, we show with concrete examples that such a group-theoretical organizing principle is essential in deciphering the complexity of the two-electron-DQD (2e-DQD) spectra arising from the interplay of both the VDOF and the selective suppression of spectral energy gaps associated with the emergence of Wigner molecules in the strong-correlation regime. This endeavor is most desirable, given that the recent CI investigations of the WM effects on the spectra and behavior of Si qubits have been restricted [12, 29, 31, 32] to the case of a single QD, in addition to overlooking the systematic patterns arising from the underlying group theoretical properties of the valley isospin.

As concrete examples, we analyze characteristic cases of Si 2e-DQD theoretical spectra that can be associated with experimentally measured ones. In particular, we address the following cases:

1. The first-excited state in the (2,0) configuration [69] is a spin triplet with both electrons in the lower-energy valley. This case is the result of strong $e-e$ interactions which drastically quench the spin-singlet/spin-triplet energy gap, $E^{\oplus}_{\mathrm{ST}}$, within the same valley, making it smaller than the small energy gap, E_V, between the two Si valleys, i.e., $E_V > E^{\oplus}_{\mathrm{ST}}$. Related experimental situations have been reported in Refs. [31, 70]. The VFCI results concerning this case are presented in Sec. III A.

2. Another possibility concerning the (2,0) charge configuration involves the formation of the first-excited state via promotion of one electron to the higher-

energy valley. In this case, one has $E_V < E_{\rm ST}^{\oplus}$. Related experimental situations have been reported in Ref. [28, 30]. The VFCI results concerning this case are presented in Sec. III B.

3. In the (1,1) charge configuration, the first-excited state involves the promotion of one electron to the higher-energy valley and a complete set of three multiplets [containing an SU(4)-characteristic total of 16 states] are resolved by lifting their degeneracies through the application of a magnetic field. The related experimental investigation was reported in Ref. [71]. This investigation parallels the recent investigations of the 2e spectra in single bilayer graphene quantum dots [72, 73]. The VFCI results concerning this case are presented in Sec. III C.

II. METHODOLOGY

In this section, we present the mathematical formulation for the VFCI methodology. In addition, we give the definition for the Wigner parameter and the various terms that contribute to the many-body Hamiltonian. Of special interest among them are terms implementing the valley-orbit coupling and the generalized spin-valley interaction (which is a generalization for two-band materials of the spin-orbit coupling).

Before proceeding with the description of the VFCI results, we mention here that in the context of valleytronics, the valley isospin is defined by a three-dimensional vector $\widehat{\mathbf{V}}$ (in analogy with the regular spin vector $\widehat{\mathbf{S}}$) which has three projections (V_x, V_y, V_z) [in analogy with the regular-spin projections (S_x, S_y, S_z)]. The three valley projections V_q, $q = x, y, z$, obey the same Lie algebra (commutation relations) as the three spin projections S_q, $q = x, y, z$. Likewise, the valley Casimir operator is given by $\widehat{\mathbf{V}}^2 = V_x^2 + V_y^2 + V_z^2$ [with eigenvalues $\mathcal{V}(\mathcal{V}+1)$], in analogy with the regular-spin Casimir operator, $\widehat{\mathbf{S}}^2 = S_x^2 + S_y^2 + S_z^2$ [with eigenvalues $\mathcal{S}(\mathcal{S}+1)$]. An electron having $V_z = \pm 1/2$ means that it lies in the low- or high-energy valley, respectively. We further note that the same symbols $\widehat{\mathbf{S}}$, $\mathcal{S}$, S_z and $\widehat{\mathbf{V}}$, $\mathcal{V}$, V_z will be used for both the case of a single electron and for the total spin and total isospin in the case of more than a single electron. Which case applies will be obvious from the context of the associated section.

A. Wigner parameter

At zero magnetic field and in the case of a single circular harmonic QD, the degree of electron localization and Wigner-molecule pattern formation can be associated with the so-called Wigner parameter [32, 34, 44, 47],

$$R_W = Q/(\hbar\omega_0), \tag{1}$$

where Q is the Coulomb interaction strength and $\hbar\omega_0$ is the energy quantum of the harmonic potential confinement (being proportional to the one-particle kinetic energy); $Q = e^2/(\kappa l_0)$, with $l_0 = (\hbar/(m^*\omega_0))^{1/2}$ the spatial extension of the lowest state's wave function in the harmonic (parabolic) confinement. Naturally, experimental signatures for the formation of Wigner molecules are expected for values $R_W > 1$, with the WM pattern being more robust the larger the value of R_W.

As mentioned in the last paragraph of Sec. III B, the values of R_W corresponding to the Si DQDs studied in this paper are $R_W = 10.0$ when $\hbar\omega_0 = 0.40$ meV and $R_W = 7.07$ when $\hbar\omega_0 = 0.80$ meV.

B. The reference many-body Hamiltonian

We consider N electrons in a double quantum dot under a low magnetic field (B) (including the case of a vanishing magnetic field). The corresponding many-body Hamiltonian,

$$H_{\rm MB} = \sum_{i=1}^{N} H_{\rm TCO}(i) + \sum_{i=1}^{N}\sum_{j>i}^{N} V(\mathbf{r}_i, \mathbf{r}_j), \tag{2}$$

is the sum of a single-particle part $H_{\rm TCO}(i)$ and the two-particle interaction $V(\mathbf{r}_i, \mathbf{r}_j)$.

Naturally, for the case of electrons, the two-body interaction is given by the Coulomb repulsion,

$$V(\mathbf{r}_i, \mathbf{r}_j) = \frac{e^2}{\kappa|\mathbf{r}_i - \mathbf{r}_j|}, \tag{3}$$

where κ is the dielectric constant of the semiconductor material ($\kappa = 11.4$ for Si).

The single-particle Hamiltonian is given by

$$H_{\rm TCO} = T + V_{\rm TCO}(x, y) + g^* \mu_B B \sigma, \tag{4}$$

where we dropped the particle index i. The last term in Eq. (4) is the Zeeman interaction, with g^* being the effective Landé factor ($g^* = 2$ for Si), μ_B the Bohr magneton, B the perpendicular magnetic field, and $\sigma = \pm 1/2$ the spin projection of an individual electron.

The kinetic contribution in Eq. (4) is given by

$$T = \frac{[\mathbf{p} - (e/c)\mathbf{A}(\mathbf{r})]^2}{2m^*}, \tag{5}$$

with m^* being the in-plane effective mass ($0.191 m_e$ for Si) and the vector potential $\mathbf{A}(\mathbf{r}) = 0.5(-By\hat{\imath} + Bx\hat{\jmath})$ being taken according to the symmetric gauge, where $\mathbf{r} = x\hat{\imath} + y\hat{\jmath}$.

The external confining potential is denoted as $V_{\rm TCO}(x, y)$. For the two-dimensional DQDs considered in this paper, the confining potential is determined by the following two-center-oscillator expression: [34, 39, 40, 45–47]

$$V_{\rm TCO} = \frac{1}{2} m^* \omega_y^2 y^2 + \frac{1}{2} m^* \omega_{xk}^2 x_k'^2 + V_{\rm neck}(x) + h_k, \tag{6}$$

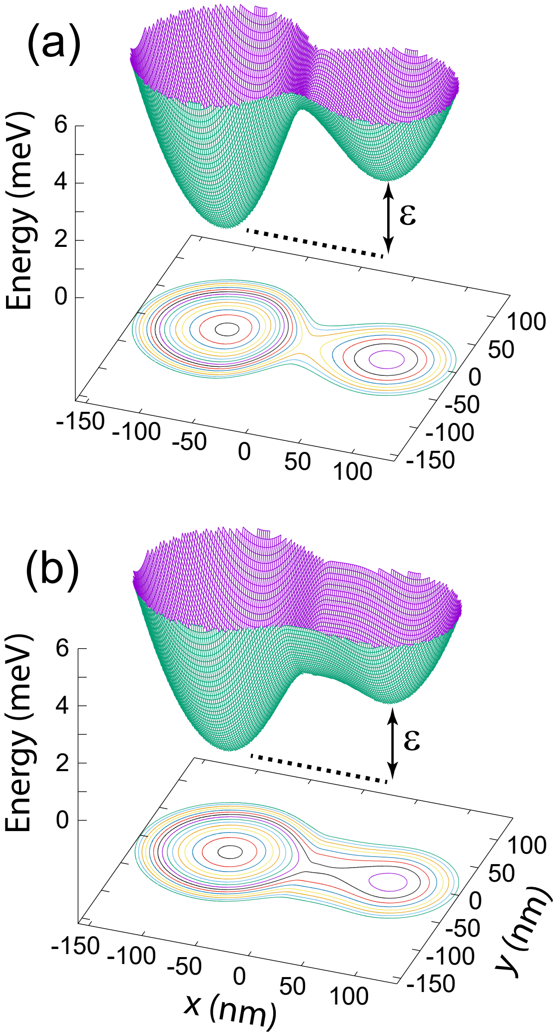

FIG. 1. The TCO external confining potential, $V_{\rm TCO}(x,y)$, including the smooth neck. (a) A high interdot barrier corresponding to a barrier control parameter of $\epsilon_1^{b,{\rm inp}} = 0.65$. (b) A lower interdot barrier corresponding to a barrier control parameter of $\epsilon_1^{b,{\rm inp}} = 0.45$. The remaining parameters are: $\hbar\omega_{x1} = \hbar\omega_{x2} = \hbar\omega_y = \hbar\omega_0 = 0.80$ meV, interdot separation $d = 150$ nm (with $-x_1 = x_2 = 75$ nm), effective mass $m^* = 0.191 m_e$ (appropriate for Si), and detuning parameter $\varepsilon = 2.71$ meV.

where $x'_k = x - x_k$ with $k = 1$ for $x < 0$ (left) and $k = 2$ for $x > 0$ (right), and the h_k's control the relative depth of the two wells, with the detuning defined as $\varepsilon = h_2 - h_1$. y denotes the coordinate perpendicular to the interdot axis (x). A notable property of $V_{\rm TCO}$ is the fact that it allows for the formation of a smooth interwell barrier between the individual wells whose height V_b can be varied independently from the interdot distance $d = x_2 - x_1$; see Fig. 1 for an illustration. The most general shapes described by $V_{\rm TCO}$ are two semiellipses connected by the smooth neck, $V_{\rm neck}(x)$. $x_1 < 0$ and $x_2 > 0$ are the centers of these semiellipses. In this paper, we take $\omega_{x1} = \omega_{x2} = \omega_y = \omega_0$ in all instances.

For the smooth neck, we use

$$V_{\rm neck}(x) = \frac{1}{2} m^* \omega_{xk}^2 \Big[\mathcal{C}_k x_k'^3 + \mathcal{D}_k x_k'^4 \Big] \theta(|x| - |x_k|), \quad (7)$$

where $\theta(u) = 0$ for $u > 0$ and $\theta(u) = 1$ for $u < 0$. The four constants $\mathcal{C}_k$ and $\mathcal{D}_k$ can be expressed via two parameters, as follows: $\mathcal{C}_k = (2 - 4\epsilon_k^b)/x_k$ and $\mathcal{D}_k = (1 - 3\epsilon_k^b)/x_k^2$, where the barrier-control parameters $\epsilon_k^b = (V_b - h_k)/V_{0k}$ are related to the height of the targeted interdot barrier (V_b, measured from the origin of the energy scale), and $V_{0k} = m^* \omega_{xk}^2 x_k^2/2$. We note that measured from the bottom of the left ($k = 1$) or right ($k = 2$) well the interdot barrier is $V_b - h_k$.

We note that in all calculations in this paper we used nonnegative values of detuning ($\varepsilon \geq 0$), namely the left well was kept in all instances lower than the right one. In addition, for convenience, we set $h_1 = 0$. In this case, it was advantageous to use a modified barrier-control parameter $\epsilon_1^{b,{\rm inp}}$ as an input parameter. Specifically, ϵ_1^b and $\epsilon_1^{b,{\rm inp}}$ are related as $\epsilon_1^b = \epsilon_1^{b,{\rm inp}}(V_{02} + \varepsilon)/V_{01}$.

Neglecting the term $V_{\rm neck}$ for the smooth neck, the eigenstates of $H_{\rm TCO}$ at $B = 0$ are used to construct the space orbitals $\varphi_j(x,y)$ of the single-particle basis employed in the CI method; see Eq. (9) below. How to solve for the eigenvalues and eigenstates of the ensuing auxiliary Hamiltonian,

$$H_{\rm aux} = \frac{\mathbf{p}^2}{2m^*} + \frac{1}{2} m^* \omega_y^2 y^2 + \frac{1}{2} m^* \omega_{xk}^2 x_k'^2 + h_k, \quad (8)$$

is described in Appendix A.

The modularity of the formulation expressed in Eqs. (2)-(8) above, endows our methodology with a large measure of flexibility and versatility, thus enabling construction of basis sets which can be used in investigations of the many-body physics of a variety of model devices, including multiple-coupled (electron or hole) quantum dots (e.g., exchange-only qubits [74]) with various sizes and shapes – described through variations of the frequencies defining the parabolic confinements ω_x, ω_y, see Eqs. (6)-(8) – which in the limit of strong anisotropy, e.g., large ω_x/ω_y, permit investigations of transitions from two-dimensional to one-dimensional (or quasi-one-dimensional) wire-like quantum-dot geometries. The lower symmetry of a wire (quasi-one-dimensional) or an ellipsoidally distorted confinement, together with physical parameters characterizing the material (e.g., effective mass and dielectric constant) that yield a larger R_W, are expected to enhance the formation of Wigner-molecule structures. We mention here that a strongly anisotropic GaAs DQD three-electron hybrid qubit was analyzed using our methodology in Refs. [46, 47], while systems of two, three, and four ultracold neutral atoms trapped in coupled quasi-linear optical traps were investigated with our methodology in Refs. [50, 51].

Finally, the Hamiltonian term implementing the spin-isospin coupling is described in Sec. II D, after the introduction in the next section of the σ_q and τ_q, $q = x, y, z$, Pauli matrices that correspond to the regular spin and to the valley isospin, respectively.

C. The valleytronic FCI approach

The band structure of crystalline silicon (having a covalently-bonded, cubic, diamond lattice structure) is known to exhibit in the conduction band, electron states that show six equivalent (degenerate) minimum energies, associated with crystal momenta ($\mathbf{k}$) that are 0.85 of the way to the Brillouin-zone boundary; these six states are termed "valleys" [75–79]. In nanoscale devices the degeneracy of the valleys is broken by various effects, including strain, confinement effects (such as lattice mismatch and/or abruptness of the interface between the nano-feature and the confining material) and electric-field effects. Due to strain in Si/SiGe quantum wells and (interfacial) quantum dots (in particular, in heterostructure semiconductors) [78], and higher subband quantization energy in MOS devices [79], the energies of the (four) in-plane valleys are raised, resulting in a remaining double (two-fold) degeneracy (in the direction normal to the dot's plane), which itself has been shown [1] to be lifted by electronic confinement due to electric field and the effects of the QD boundary structure (including interfacial disorder and/or steps for Si/SiGe quantum dots). In this paper, as is the case for the general practice for the Si DQDs, we consider that the VDOF consists only of the low-energy two-fold band.

As remarked at the end of the introductory section, to characterize and classify the VDOF of the two remaining valleys, we introduce in this paper an isospin designation that is constructed in analogy [including the SU(2) algebra generated by the i-multiplied Pauli matrices] with that of the regular spin of the electrons (replacing $\widehat{\mathbf{S}}$ with $\widehat{\mathbf{V}}$ when referring to the VDOF). Obviously, in the absence of two-body interactions, the occupation of the single-particle energy states [80] in the dots would depend on an interplay between the confinement (including an applied magnetic field) and the valley effects. For the case of valley degeneracy or near-degeneracy (determined by the intervalley-splitting, E_V, also referred to as valley gap), and with a confinement gap (that is the energy spacing between successive confinement–induced single-particle states) which is much larger than E_V, this interplay results in "doubling" of the spectrum (two near-degenerate states for each confinement state, each corresponding to a different valley).

As aforementioned, we use the method of configuration interaction for determining the solution of the many-body problem specified by the Hamiltonians $H_{\rm MB}+H_{\rm VS}$, $H_{\rm MB}+H_{\rm VS}+H_{\rm VOC}$, or $H_{\rm MB}+H_{\rm VS}+H_{\rm SIC}$ (these Hamiltonians were defined in Sec. II).

In the CI method, one writes the many-body wave function $\Phi_N^{\rm CI}(\mathbf{r}_1,\mathbf{r}_2,\ldots,\mathbf{r}_N)$ as a linear superposition of Slater determinants $\Psi^N(\mathbf{r}_1,\mathbf{r}_2,\ldots,\mathbf{r}_N)$ that span the many-body Hilbert space and are constructed out of the single-particle *spin-isospin-orbitals* [81]

$$\begin{aligned}
\chi_j(\mathbf{r}) &= \varphi_j(x,y)\alpha\zeta, && \text{if} \quad 1\le j\le K,\\
\chi_j(\mathbf{r}) &= \varphi_{j-K}(x,y)\beta\zeta, && \text{if} \quad K< j\le 2K,\\
\chi_j(\mathbf{r}) &= \varphi_{j-2K}(x,y)\alpha\eta, && \text{if} \quad 2K< j\le 3K,\\
\chi_j(\mathbf{r}) &= \varphi_{j-3K}(x,y)\beta\eta, && \text{if} \quad 3K< j\le 4K,
\end{aligned} \tag{9}$$

where $\alpha(\beta)$ denote up (down) spins, $\zeta(\eta)$ denote up (down) isospins [i.e., electrons in the first (second) valley], and the spatial orbitals $\varphi_j(x,y)$ are given by the K lowest-energy solutions of the auxiliary single-particle Hamiltonian in Eq. (8). For clarity and convenience, these solutions are sorted in ascending energy.

We note that, in analogy with the case of the Pauli spin matrices σ_x, σ_y, and σ_z, three additional Pauli matrices τ_x, τ_y, and τ_z, associated with the valley isospin, can be defined, yielding the relations $\tau_x\zeta=\eta$, $\tau_x\eta=\zeta$, $\tau_y\zeta=i\eta$, $\tau_y\eta=-i\zeta$, $\tau_z\zeta=\zeta$, and $\tau_z\eta=-\eta$.

Making contact with the effective mass theory (continuum model) [62] for semiconductor heterostructures, we identify the $\varphi_j(x,y)$'s as the envelope functions of this theory as applied to gated finite-size semiconductor and carbon nanostructures [63].

The isospin functions ζ and η are orthornormal, in analogy with the regular spin functions α and β. Unlike the exact orthornormality of α and β, however, the orthornormality of ζ and η is an approximate property, which nonetheless is highly accurate when the confining (gate) potentials vary slowly over the distance defined by the lattice constant a of the material. This follows from the fact [82] that the Bloch functions that multiply the envelope functions in the effective-mass approach are varying rapidly in space with a period determined by the material's lattice constant a, whereas the envelope functions vary slowly over the much larger extent defined by the size of the nanostructure.

Specifically, the many-body wave function is written as

$$\Phi_{N,q}^{\rm CI}(\mathbf{r}_1,\ldots,\mathbf{r}_N)=\sum_I C_I^q \Psi_I^N(\mathbf{r}_1,\ldots,\mathbf{r}_N), \tag{10}$$

where

$$\Psi_I^N=\frac{1}{\sqrt{N!}}\begin{vmatrix} \chi_{j_1}(\mathbf{r}_1) & \ldots & \chi_{j_N}(\mathbf{r}_1)\\ \vdots & \ddots & \vdots \\ \chi_{j_1}(\mathbf{r}_N) & \ldots & \chi_{j_N}(\mathbf{r}_N)\end{vmatrix}, \tag{11}$$

and the master index I counts the number of arrangements $\{j_1,j_2,\ldots,j_N\}$ under the restriction that $1\le j_1< j_2<\ldots<j_N\le 4K$. I specifies the dimension of the many-body Hilbert space spanned by the basis of Slater determinants. Of course, $q=1,2,\ldots$ counts the excitation spectrum, with $q=1$ corresponding to the ground state.

The many-body Schrödinger equation

$$\mathcal{H}\Phi_{N,q}^{\rm CI}=E_{N,q}^{\rm CI}\Phi_{N,q}^{\rm CI} \tag{12}$$

transforms into a matrix diagonalization problem, which yields the coefficients C_I^q and the eigenenergies $E_{N,q}^{\rm CI}$. Because the resulting matrix is sparse, we implement its numerical diagonalization employing the well known ARPACK solver [83] which uses implicitly restarted Arnoldi methods. Convergence of the many-body solutions is guaranteed by using a large enough value for the dimension K of the single-particle basis; we used here $K \sim 50$. The attribute "full" is usually used for such well converged CI solutions, which naturally contain all possible n-particle $-$ n-hole basis Slater determinants, n being an integer.

The matrix elements $\langle \Psi_I^N | H_{\rm MB} + H_{\rm VS} + H_{\rm SIC} | \Psi_J^N \rangle$, or the simpler ones $\langle \Psi_I^N | H_{\rm MB} + H_{\rm VS} | \Psi_J^N \rangle$, between the basis Slater determinants [see Eq. (11)] are calculated using the Slater–Condon rules [45, 84–86]; for the spin- and/or isospin-dependent Hamiltonian terms $H_{\rm VS}$ and $H_{\rm SIC}$, see Sec. II D below.

Naturally, an important ingredient in this respect are the matrix elements of the two-body interaction,

$$\int_{-\infty}^{\infty} \int_{-\infty}^{\infty} d\mathbf{r}_1 d\mathbf{r}_2 \varphi_i^*(\mathbf{r}_1) \varphi_j^*(\mathbf{r}_2) V(\mathbf{r}_1, \mathbf{r}_2) \varphi_k(\mathbf{r}_1) \varphi_l(\mathbf{r}_2), \tag{13}$$

in the basis formed out of the single-particle spatial orbitals $\varphi_i(\mathbf{r})$, $i = 1, 2, \ldots, K$ [see Eq. (9)]. In our approach, these matrix elements are determined numerically and stored separately.

Taken individually, the Slater determinants Ψ_I^N [see Eq. (11)] preserve the third projections S_z and V_z, but not necessarily the square $\hat{\mathbf{S}}^2$ and $\hat{\mathbf{V}}^2$ of the total spin and total isospin. However, because $\hat{\mathbf{S}}^2$ and $\hat{\mathbf{V}}^2$ commute with the many-body Hamiltonians $H_{\rm MB}$ and $H_{\rm MB} + H_{\rm VS}$, the associated exact many-body solutions are eigenstates of both $\hat{\mathbf{S}}^2$ and $\hat{\mathbf{V}}^2$ with eigenvalues $\mathcal{S}(\mathcal{S}+1)$ and $\mathcal{V}(\mathcal{V}+1)$, respectively.

With the VFCI solution at hand [Eq. (10), which numerically approximates the exact many-body one], one calculates the expectation values

$$\langle \Phi_N^{\rm CI} | \hat{\mathbf{S}}^2 | \Phi_N^{\rm CI} \rangle = \sum_I \sum_J C_I^* C_J \langle \Psi_I^N | \hat{\mathbf{S}}^2 | \Psi_J^N \rangle, \tag{14}$$

and similarly for $\hat{\mathbf{V}}^2$; for simplicity, in Eq. (14), we dropped the index q. The ARPACK diagonalization provides the numerical C_I and C_J coefficients, and the matrix elements of $\hat{\mathbf{S}}^2$ and $\hat{\mathbf{V}}^2$ between the basis Slater determinants are determined by using the relations

$$\hat{\mathbf{S}}^2 \Psi_I^N = \left[(N_\alpha - N_\beta)^2/4 + N/2 + \sum_{i<j} \varpi_{ij} \right] \Psi_I^N, \tag{15}$$

and

$$\hat{\mathbf{V}}^2 \Psi_I^N = \left[(N_\zeta - N_\eta)^2/4 + N/2 + \sum_{i<j} \varpi_{ij}^{\rm iso} \right] \Psi_I^N, \tag{16}$$

where the operator ϖ_{ij} ($\varpi_{ij}^{\rm iso}$) interchanges the spins (isospins) of fermions i and j provided that these spins (isospins) are different; N_α (N_ζ) and N_β (N_η) denote the number of spin-up (isospin-up) and spin-down (isospin-down) fermions, respectively. Formula (16) for the square of the isospin is introduced here in complete analogy with the familiar expression [87] for the square of the regular spin.

Furthermore, the VFCI expectation values for the total-spin projection are calculated using the formula:

$$\langle \Phi_N^{\rm CI} | S_z | \Phi_N^{\rm CI} \rangle = \sum_I C_I^* C_I \langle \Psi_I^N | S_z | \Psi_I^N \rangle, \tag{17}$$

and similarly for the total-isospin projection V_z.

We note that the VFCI solutions of the reference many-body Hamiltonian (2), as well those of the $H_{\rm MB} + H_{\rm VS}$ Hamiltonian, preserve automatically the spin and isospin quantum numbers as long as they are not members of an energy degeneracy. To enforce that the VFCI solutions of these Hamiltonians preserve the spin and isospin quantum numbers in all instances, including the case of degeneracies, we add to $H_{\rm MB}$, or to $H_{\rm MB} + H_{\rm VS}$, a very small perturbing term $H_{\rm SIC}$, which lifts the energy degeneracies to an imperceptible amount, but it produces the desired effect. An example of the success of this approach is presented in Table I in Appendix B, where the deviations of the expectation values of the $\hat{\mathbf{S}}^2$ and $\hat{\mathbf{V}}^2$ from the expected $\mathcal{S}(\mathcal{S}+1)$ and $\mathcal{V}(\mathcal{V}+1)$ integer values, i.e., 0 or 2 for two electrons in both cases, appear at most in the fifth decimal point for all the 16 states listed. Similarly, the deviations of the expectation values of S_z and V_z from the expected ± 1 or 0 integer values for two electrons appear again at most in the fifth decimal point for all the 16 states listed.

D. The spin-isospin coupling and the valley splitting

Motivated by the large body of experimental evidence [21, 28, 71, 88] that a spin-valley coupling is operational in Si qubits, we implement in the VFCI an appropriate spin- and isospin-dependent coupling, referred to in this paper as spin-isospin coupling, by adding the following (one-body) term in the many-body Hamiltonian:

$$H_{\rm SIC} = H_{\rm VOC} + H_{\rm SVOC}, \tag{18}$$

where

$$H_{\rm VOC} = \sum_{i=1}^N \Delta e^{i\phi_0} \widehat{O}(x,y) \tau_x(i), \tag{19}$$

and

$$H_{\rm SVOC} = \sum_{i=1}^N \Delta e^{i\phi_0} \widehat{O}(x,y) \sigma_x(i) \tau_x(i). \tag{20}$$

with Δ being the strength and ϕ_0 being the phase of the coupling parameter. When calculating the $\langle \chi_{j_1}(\mathbf{r}) | H_{\rm SIC} | \chi_{j_2}(\mathbf{r}) \rangle$ matrix elements, we approximate the integrals over the space variables as

$\langle\varphi_{j_1}(x,y)|\widehat{O}(x,y)|\varphi_{j_2}(x,y)\rangle \approx \delta_{j_1-j_2,\pm1}$, where $1 < j_1$ or $j_2 \leq K$ [89].

We note that the first term, $H_{\rm VOC}$, in Eq. (18) implements a pure intervalley coupling (referred to often as valley-orbit coupling) by keeping the spin indices unaltered. The second term, $H_{\rm SVOC}$, in Eq. (18) flips both the valley and regular-spin indices, thus corresponding to a combined VOC and spin-orbit coupling; it is referred to as spin-valley-orbit coupling, or simply as spin-valley coupling. A pure $H_{\rm VOC}$ coupling is implented in the VFCI by restricting the Hilbert space to the sector that preserves the total spin projection, S_z. To implement in addition the $H_{\rm SVOC}$ coupling, one needs to remove all restrictions on S_z and V_z when building the basis of Slater determinants. This requires substantially larger Hilbert spaces, e.g., for the case of $K = 54$ employed in our calculations, the dimension of the Hilbert space (the master index I) increases from 5778 (using an $S_z = 0$ restriction only) to 23220 basis Slater determinants (with no S_z and V_z restrictions).

The spin-valley coupling defined in Eq. (20) contains both the Pauli σ (regular spin) and the Pauli τ (isospin) matrices, as is appropriate for a two-band material (see Ref. [90] for the case of graphene). Such a definition is a generalization of the familiar Rashba and Dresselhaus spin-orbit expressions for one-band materials.

Finally, the valley gap (valley splitting) is described by the following (one-body) Hamiltonian term:

$$H_{\rm VS} = \sum_{i=1}^{N} \frac{E_V}{2}\tau_z(i). \tag{21}$$

III. RESULTS

In this section, we present VFCI results for the low energy spectra of Si 2e-DQD devices with parameters similar to those of actual quantum qubits investigated experimentally and reported in recent and current literature. Prior to presentation and discussion of the results of our calculations, it is pertinent to comment here in some detail about certain aspects of our calculations, originating from the intrinsic properties of the material (silicon) used in making the DQD qubits addressed by our study. To this end we focus specifically on the valletronic nature of the electronic structure of the Si quantum dots studied here, and the terminology used in characterizing and discussing their properties.

Moving next to the studying of the many-body states in Si QDs, we start by considering a many-body reference Hamiltonian, $H_{\rm MB}$, which includes the confinement potential defining the quantum dots, applied magnetic fields, and the interelectron Coulomb potential, assuming the case of a full valley degeneracy; see Sec. II B. The valley splitting is then included by adding a one-body Hamiltonian term $H_{\rm VS}$; see Eq. (21) in Sec. II D. Furthermore, from among others, we consider in this paper two other one-body interaction terms that are of particular interest (for details, see Sec. II D). Namely, we consider a spin- and isospin-dependent coupling, $H_{\rm SIC}$, that consists of two contributions: (i) A contribution that acts only within the isospin (valley) degree of freedom and mixes the valleys, but not the real spins; this term is referred to as the valley-orbit coupling, $H_{\rm VOC}$, in analogy with the real spin-orbit interaction and (ii) A contribution, $H_{\rm SVOC}$, that couples simultaneously both the (real) spin and isospin degrees of freedom, termed as the spin-valley-orbit coupling, or simply the spin-valley coupling.

The VFCI calculations for the total energies discussed in Secs. III A and III B were carried out in the Hilbert-space sector specified by the total-spin projection $S_z = 0$. This is sufficient for the purpose of these sections, because the total energies of the reference many-body Hamiltonian, $H_{\rm MB}$, as well as its extensions $H_{\rm MB} + H_{\rm VS}$ and $H_{\rm MB} + H_{\rm VS} + H_{\rm VOC}$ that include the valley splitting (VS) and/or the pure valley-orbit coupling (VOC), do not depend on the value ±1 or 0 of the total-spin projection. In cases when VFCI eigenstates with $S_z = \pm1$ values need to be considered, e.g., for counting the degeneracy of the states participating in a given multiplet (see Sec. III A 3 below), an explicit mention of the VFCI results will be made without showing the corresponding energy spectra. On the other hand, no restriction on the total-spin projection S_z (and on the total-isospin projection V_z as well) is placed in Sec. III C where the full spin-isospin coupling, $H_{\rm SIC}$, which flips both the valley-isospin and regular-spin indices, is taken into consideration.

A. First-excited state with both electrons in the same valley

1. *Low-energy spectra*

The VFCI lowest energy spectrum in the transition region between the (1,1) and the (2,0) charge configurations, as a function of the detuning, ε, is displayed in Fig. 2. A weaker individual-dot confinement of $\hbar\omega_0 = 0.40$ meV was employed for both dots, along with an interdot separation of $d = 150$ nm [91]. The valley gap was assumed to be $E_V = 100$ μeV $= 24.180h$ GHz, whereas the in-plane Si effective mass was taken as $0.191m_e$ and the dielectric constant of Si as $\kappa = 11.4$. A high interdot barrier was implemented in Fig. 2(a) by setting the input interdot-barrier parameter to $\epsilon_1^{b,\rm inp} = 0.65$ (see Sec. II B for the meaning of this input barrier-controlling parameter). A low interdot barrier was implemented in Fig. 2(b) by setting $\epsilon_1^{b,\rm inp} = 0.50$. [For the definition and an illustration of the two-center-oscillator (TCO) two-well confinement employed in this paper, see Eq. (6) and Fig. 1 in Sec. II B, respectively.]

The symbols $\oplus$, ⓪, and $\ominus$ indicate states with both electrons in the low-energy valley, with the electrons in different valleys, and with both electrons in the high-energy valley, respectively. The spin-isospin coupling was

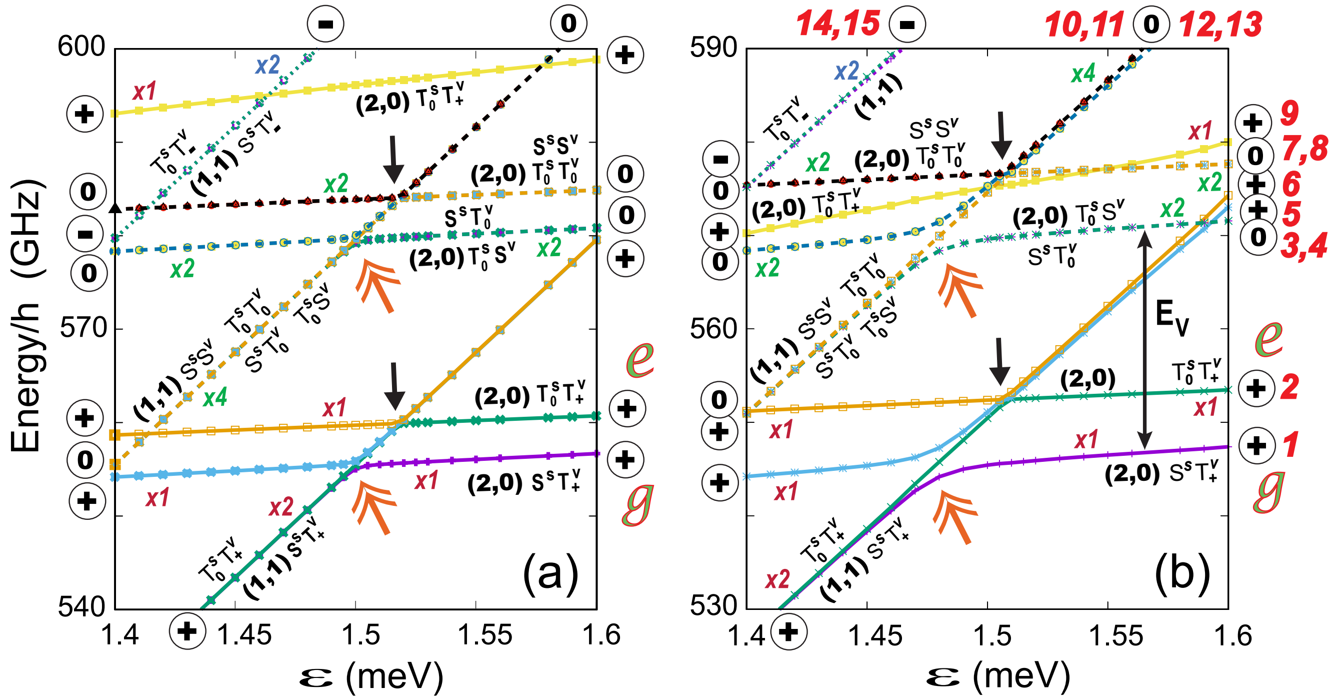

FIG. 2. The case with $E_{\rm ST}^{\oplus} < E_V$. VFCI lowest energy spectrum, associated with the Hamiltonian $H_{\rm MB}+H_{\rm VS}$ (see text), for the case of a 2e Si DQD with a weaker individual-dot confinement, $\hbar\omega_0 = 0.40$ meV $= 96.719h$ GHz, for both dots, at a vanishing magnetic field, $B = 0$. The spectrum is plotted in the transition region between the (1,1) and the (2,0) charge configurations, as a function of the detuning, ε, and for a total-spin projection $S_z = 0$. The interdot separation was taken as $d = 150$ nm, and the valley gap was set as $E_V = 100$ μeV $= 24.180h$ GHz. *The first excited state in the (2,0) configuration has both electrons in the same lowest-energy valley [the script letters g and e, outside the right borders of panels (a) and (b), denote the ground and first-excited states in the (2,0) configuration, respectively].* The energy difference between the e and g states at $\varepsilon = 1.60$ meV equals $E_{\rm ST}^{\oplus} \approx 4.05h$ GHz in panel (a) and $E_{\rm ST}^{\oplus} \approx 6.09h$ GHz in panel (b). (a) A high interdot barrier was implemented by setting $\epsilon_1^{b,{\rm inp}} = 0.65$ (see Sec. II B for the meaning of the input barrier-controlling parameter). (b) A low interdot barrier was implemented by setting $\epsilon_1^{b,{\rm inp}} = 0.50$. The in-plane Si effective mass was taken as $0.191m_e$ and the dielectric constant as $\kappa = 11.4$. The symbols $\oplus$, ⓪, and $\ominus$ indicate states with both electrons in the low-energy valley (with $V_z = +1$), with the electrons in different valleys (with $V_z = 0$), and with both electrons in the high-energy valley (with $V_z = +1$), respectively. The 5 near-horizontal lines correspond to the (2,0) charge configuration (as indicated). The three quasi-parallel lines with a larger slope correspond to the (1,1) charge configuration (as indicated). The valley-orbit and spin-isospin couplings were neglected, and as a result all states are associated with good total spin $[\mathcal{S}(\mathcal{S}+1),S_z]$ and valley isospin $[\mathcal{V}(\mathcal{V}+1),V_z]$ quantum numbers (as indicated). The symbols made from a combination of the capital letters S and T have the following meaning: A capital S denotes a singlet state, whereas a capital T denotes a triplet state. The subscripts $\pm$ denote an $S_z = \pm 1$ spin projection or a $V_z = \pm 1$ valley projection, respectively, whereas a subscript 0 denotes an $S_z = 0$ or $V_z = 0$ projection. A superscript "s" denotes the regular spin, whereas a superscipt "v" denotes the valley isospin. "xn" (with $n = 1$, 2, or 4) denotes the n-fold degeneracy associated with a given energy curve; red color is used for the $\oplus$ states (with $V_z = +1$), green color for the ⓪ states (with $V_z = 0$), and blue color for the $\ominus$ ones (with $V_z = -1$). The double-headed red arrows indicate avoided crossings between two spin singlet states in the transition from the (1,1) to the (2,0) configuration. These crossings are underdeveloped in the case of a high interdot barrier [see panel (a)], but become pronounced for low interdot barriers [see panel (b)]. The single-head black arrows indicate avoided crossings between two spin triplet states in the transition from the (1,1) to the (2,0) configuration. These crossings are underdeveloped in both the cases of a high interdot barrier [see panel (a)], as well as a low interdot barrier [see panel (b)]. The numerical labels in red outside the border of panel (b) are used to identify the energy curves by numbering them. This numbering is used in the discussion in the text of Sec. III A; in addition, it will assist with the correspondence between charge densities (see Fig. 3) and the states whose energies are plotted here. In all figures and the values mentioned in the text, the energies are referenced to $2\hbar\sqrt{\omega_0^2+\omega_c^2/4}$, where $\omega_c = eB/(m^* c)$ is the cyclotron frequency. The dots in this figure and in all subsequent figures are equidistant from the origin.

neglected, and as a result all states are associated with good total spin ($\mathcal{S}$, S_z) and valley isospin ($\mathcal{V}$, V_z) quantum numbers, as indicated via the symbols made from a combination of the capital letters S and T. These symbols have the following meaning: A capital S denotes a singlet state, whereas a capital T denotes a triplet state [92]. The subscripts $\pm$ denotes an $S_z = \pm 1$ or $V_z = \pm 1$ projection, respectively, whereas a subscript 0 denotes an $S_z = 0$ or $V_z = 0$ projection. A superscript “s” denotes the regular spin, whereas a superscipt “v” denotes the valley isospin. The symbol “xn” (with $n = 1$, 2, or 4) denotes the n-fold degeneracy associated with a given energy curve; red color is used for the $\oplus$ states (with $V_z = +1$), green color for the ⓪ states (with $V_z = 0$), and blue color for the $\ominus$ ones (with $V_z = -1$). Finally, the numerical labels in red outside the border of Fig. 2(b) are used to identify the energy curves by numbering them.

The energy difference at $\varepsilon = 1.6$ meV between the (2,0) states indicated as e [first-excited state, no. 2 in Fig. 2(b)] and g [ground state, no. 1 in Fig. 2(b)] equals $E_{\rm ST}^{\oplus}$. The energy difference at $\varepsilon = 1.6$ between the (2,0) lines indicated in Fig. 2(b) as nos. 3,4 (a doubly degenerate pair) and the line no. 1 (ground state) equals E_V. E_V equals also the energy difference between the middle and any outer of the three (1,1) parallel lines. It is clear that $E_{\rm ST}^{\oplus} < E_V$ for the case illustrated in this section.

As is apparent from Fig. 2, the VFCI solutions are able to capture both the (1,1) and (2,0) charge configurations, whether ground or excited states, and their interconversion as a function of the detuning. Specifically, the 5 quasi-parallel and quasi-horizontal lines correspond to the (2,0) charge configuration (as indicated), whereas the 3 quasi-parallel lines with a large slope correspond to the (1,1) charge configuration (again, as indicated). Of particular interest are the avoided crossings (marked by double-head red arrows) between two spin singlet states in the transition from the (1,1) to the (2,0) configuration. These crossings are underdeveloped in the case of a high interdot barrier [see Fig. 2(a)], but become pronounced for low interdot barriers [see Fig. 2(b)]. The single-head black arrows indicate avoided crossings between two spin triplet states in the transition from the (1,1) to the (2,0) configuration, which however remain underdeveloped in both the cases of a high interdot barrier [see Fig. 2(a)], as well as a low interdot barrier [see Fig. 2(b)].

A main conclusion form the VFCI results in Fig. 2 is that, for a given V_z, the energy gaps between the spin singlet and and spin triplet states in the (2,0) configuration are drastically suppressed compared to the orbital (single-particle) gap of $\hbar\omega_0 = 0.40$ meV $= 96.719h$ GHz associated with the non-interacting limit; see, e.g., the spin-singlet−spin-triplet gap, $E_{\rm ST}^{\oplus}$, at $\varepsilon = 1.60$ meV between the ground and first-excited states (denoted as g and e, respectively), which is $E_{\rm ST}^{\oplus} \approx 4.05h$ GHz in Fig. 2(a) and $E_{\rm ST}^{\oplus} \approx 6.09h$ GHz in Fig. 2(b). This quenching of the gaps, which recently was observed experimentally in Si [31, 70] (but also in GaAs [9]) DQD qubits, is the result of strong-electron correlations and of the formation of Wigner molecules. Namely, the ensuing spatial localization of the electrons within the left or right QD reduces the Coulomb repulsion between them, a process that leads to the convergence of the energies between the states with symmetric and antisymmetric space parts. For two electrons, this process mimicks the dissociation of the natural H_2 molecule, and it was discovered earlier in the case of GaAs quantum dots [18, 39, 40, 44, 52, 93].

2. *Charge densities*

The formation of WMs (in the case of asymmetric confinements) is graphically illustrated through the charge densities, which are displayed in Fig. 3. For the reader's convenience and for helping with establishing the correspondence between the charge densities in Fig. 3 and the states whose energies are plotted in Fig. 2, we assigned to the VFCI energy curves the numbers in red displayed outside the border of Fig. 2(b). These numbers are used in this section below.

To facilitate the identification and elucidation of the main trends, we display, along with the charge densities, the VFCI calculated electron occupancies (red lettering) in the left and right wells of the DQD (rounded to the second decimal point). [These VFCI occupations are further rounded to the closest integer in order to obtain the n_L's and n_R's ($n_L + n_R = 2$) used in the notation (n_L, n_R) [69] for the charge configurations.] Naturally, the charge densities are normalized to the total number of electrons, $N = 2$.

The ground-state at $\varepsilon = 1.60$ meV (curve no. 1) with a symmetric space part and both electrons in the low-energy valley (note the symbol $\oplus$ in Fig. 3) exhibits a rather well developed WM inside the left well, which is aligned parallel to the y-axis. Curve no. 2 with an antisymmetric space part and both electrons in the low-energy valley exhibits an even better developed WM due to its nodal structure; again this WM resides within the left QD and is aligned parallel to the y-axis.

Promoting one electron to the high-energy valley [states marked as ⓪] leaves the charge densities unaltered. Indeed, the density in Fig. 3(a) coincides with the densities in Fig. 3(c) (curves nos. 3 and 4), and the density in Fig. 3(b) coincide with those in Fig. 3(f) (curves nos. 7 and 8).

State no. 9 at $\varepsilon = 1.60$ meV with both electrons in the low-energy valley deviates from a pure (2,0) configuration, as is apparent from the density in Fig. 3(g). Indeed, at this point, state no. 9 starts forming an avoided crossing with state no. 5 [an (1,1) state with the same spin-isospin quantum numbers $(\mathrm{T}_0^s\mathrm{T}_+^v)$], and thus it becomes a superposition of both a (2,0) and an (1,1) configuration; this behavior is denoted with a “*” as a superscript. Note that the (2,0) component of state no. 9 is associated with a 2e-WM aligned along the x-axis. Naturally, state no. 5 is also a superposition, although weaker, of both a (2,0) and an (1,1) configuration and is denoted with a “*” as a superscript. Another state that belongs in this category is state no. 14.

The two remaining panels [i.e., Figs. 3(e,h)], corresponding to curves no. 6 at $\varepsilon = 1.60$ meV, and to the curve no. 10 at $\varepsilon = 1.56$ meV, respectively, display densities associated with an (1,1) configuration. Similar (1,1)

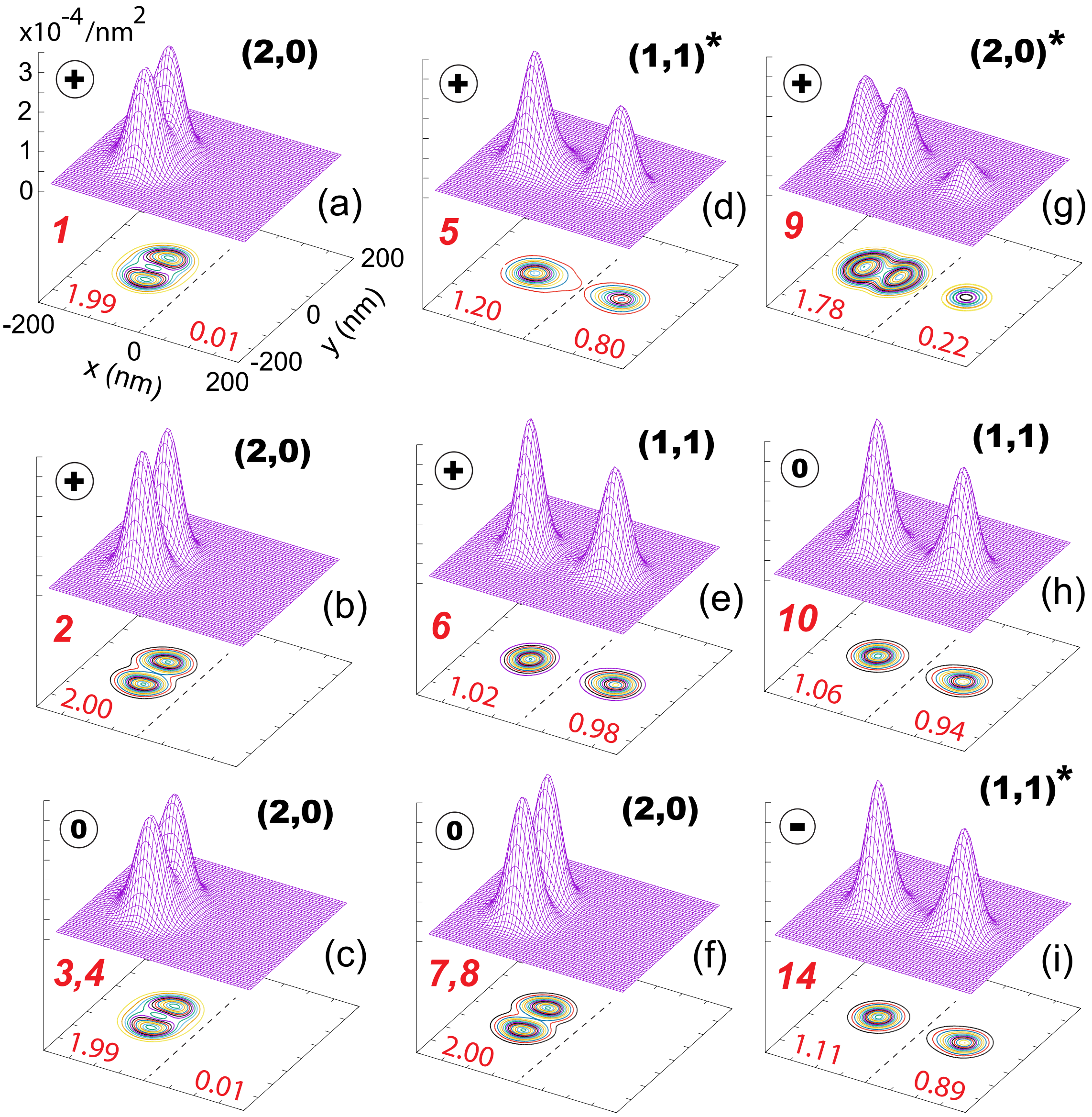

FIG. 3. Charge densities associated with the VFCI states whose energies are plotted in Fig. 2(b), at $\varepsilon = 1.60$ meV for curves nos. 1-9, at $\varepsilon = 1.56$ meV for curve no. 10, and at $\varepsilon = 1.46$ meV for curve no. 14. This is the case with a low interdot barrier that was implemented by setting $\epsilon_1^{b,\mathrm{inp}} = 0.50$ (see Sec. II B for the meaning of the input barrier-controlling parameter). The displayed thin red decimal numbers in each panel are the VFCI calculated electron occupancies in the left and right wells of the DQD. A "*" denotes a state participating in an avoided crossing, to a lesser or greater extent. The bold red numerical labels have the same meaning as those in Fig. 2(b).

densities (not shown) are also associated with curves nos. 11, 12, 13.

3. *Counting of states and the degeneracy of multiplets*

The case of the (1,1) charge configuration. For $S_z = 0$, the valleytronic FCI produces a group of 8 states with an (1,1) configuration (shown in Figs. 2 and 4) that are grouped as 2 ⊕,4 ⓪,2 ⊖. Likewise, for $S_z = +1$, the valleytronic FCI produces a group of 4 states (not shown) with an (1,1) configuration grouped as 1 ⊕,2 ⓪,1 ⊖. Finally, for $S_z = -1$, the valleytronic FCI produces another group of 4 states (not shown) with an (1,1) configuration grouped again as 1 ⊕,2 ⓪,1 ⊖. In total, one obtains 16 states that are grouped in multiplets as 4 ⊕,8 ⓪,4 ⊖.

The number of 16 states is the hallmark of a fully developed SU(4) symmetry that would be achieved in the 2e-VFCI in the absence of any spin-isospin coupling (i.e., neglecting the H_{VOC} and/or H_{SIC} terms) and for the case of a vanishing valley gap ($E_V = 0$). These sixteen states are the product of the four spin states (one singlet, S^s, and three triplets, $\mathrm{T}^s_\pm$ and T^s_0) and the four valley isospin states (one singlet, S^v, and three triplets, $\mathrm{T}^v_\pm$ and T^v_0). Their quantum numbers are explicitly given as follows: there are 6 antisymmetric combinations $\mathrm{S}^s\mathrm{T}^v_+$, $\mathrm{S}^s\mathrm{T}^v_0$, $\mathrm{S}^s\mathrm{T}^v_-$, $\mathrm{T}^s_+\mathrm{S}^v$, $\mathrm{T}^s_0\mathrm{S}^v$, $\mathrm{T}^s_-\mathrm{S}^v$ and 10 symmetric combinations $\mathrm{S}^s\mathrm{S}^v$, $\mathrm{T}^s_+\mathrm{T}^v_+$, $\mathrm{T}^s_+\mathrm{T}^v_0$, $\mathrm{T}^s_+\mathrm{T}^v_-$, $\mathrm{T}^s_0\mathrm{T}^v_+$, $\mathrm{T}^s_0\mathrm{T}^v_0$, $\mathrm{T}^s_0\mathrm{T}^v_-$, $\mathrm{T}^s_-\mathrm{T}^v_+$, $\mathrm{T}^s_-\mathrm{T}^v_0$, $\mathrm{T}^s_-\mathrm{T}^v_-$.

In the case of a single elliptic dot, these 16 SU(4)-states, that form the lowest-energy part of the spectrum, organize in two multiplets [94] in analogy with the case of an SU(4) Heisenberg lattice dimer (see (a) in Ref. [65] and Ref. [95]), six of them in one multiplet with a symmetric space part and the remaining ten in a second higher-energy multiplet with an antisymmetric space part [96].

In the case of two well separated QDs in the strict SU(4) limit, the energy gap between space-symmetric and space-antisymmetric multiplets vanishes due to a vanishing left-right spatial overlap, and this yields a total of 16 degenerate SU(4)-states in the (1,1) configuration. However, in Si DQDs, this degeneracy is lifted due to the independent emergence of a valley gap that results from finite-size effects, and the SU(4) symmetry is lowered to an SU(2) × SU(2) one, characterized by the 4 ⊕,8 ⓪,4 ⊖ multiplet organization discussed above.

The case of the (2,0) and (0,2) charge configurations. From Fig. 2, it can easily be seen that, according to the VFCI results, the hallmark number of the 16 states of the SU(4) ⊃ SU(2) × SU(2) chain is preserved in the (2,0) configuration; simply the exhange gap J between the space-symmetric and space-antisymmetric states acquires a non-vanishing finite value. For example, as seen in Fig. 2(a), the two degenerate ⊕ states, $\mathrm{S}^s\mathrm{T}^v_+$ and $\mathrm{T}^s_0\mathrm{T}^v_+$, in the (1,1) configuration transition into the g and e states in the (2,0) configuration, exhibiting a gap of 4.05h GHz at $\varepsilon = 1.60$ meV. A similar transition applies also in the case of the four degenerate (1,1) states in the ⓪ manifold, which splits into two doubly degenerate manifolds in the (2,0) configuration. Finally, a transition of the doubly degenerate ⊖ manifold of the (1,1) configuration to two non-degenerate states in the (2,0) configuration is not shown in Fig. 2(a), but it was observed in our extensive VFCI computational results.

Our verification in the VFCI spectra of the presence of the 16 hallmark states associated with the SU(4) ⊃ SU(2) × SU(2) chain contrasts with the counting from a Hubbard two-site modeling [97] of a Si 2e-DQD that incorporates the VDOF. Indeed, instead of the expected number of 16 states, the model in Ref. [97] allows only for 6 states in the (2,0) configuration. This incomplete conclusion follows directly from the assumption that each Hubbard site has one level only, an assumption that does not allow the construction of 2e antisymmetric space wave functions in the case of the (2,0) configuration.

We note that adding a spin-isospin coupling term (including one or both contributions, see Sec. II D) in the many-body Hamiltonian will lift the degeneracies illustrated in the spectra of Fig. 2, however, the overall organization of such Si-DQD spectra will be traceable back to that in Fig. 2, as long as the strength of the spin-isospin coupling is not extreme.

B. First-excited state with electrons in different valleys

We turn now to the case when the first-excited state in the (2,0) configuration has one electron in the low-energy valley and the second electron in the higher-energy valley, i.e., it exhibits a valley isospin projection $V_z = 0$ (denoted as ⓪). The evolution of the VFCI low-energy spectra in this case is investigated in Fig. 4, as a function of the height of the interdot barrier [Fig. 4(a) and Fig. 4(b)] and in response to the inclusion of the pure intervalley-coupling Hamiltonian term, $H_{\rm VOC}$ (see Sec. II D), in the Hamiltonian $H_{\rm MB} + H_{VS}$ [Fig. 4(c)].

Specifically, for a total-spin projection $S_z = 0$, Fig. 4 displays, as a function of the detuning, ε, the VFCI low-energy spectrum for a Si 2e-DQD with a stronger individual-dot confinement of $\hbar\omega_0 = 0.80$ meV in the transition region between the (1,1) and the (2,0) charge configurations. The valley gap was taken as $E_V = 60$ μeV $= 14.508h$ GHz. As in the weaker individual-dot-confinement case of Fig. 2, the interdot separation was set to $d = 150$ nm, the in-plane Si effective mass was taken as $0.191m_e$, and the dielectric constant as $\kappa = 11.4$. A high interdot barrier ($\epsilon_1^{b,\rm inp} = 0.65$) was chosen for Fig. 4(a), whereas a low interdot barrier ($\epsilon_1^{b,\rm inp} = 0.35$) was used for Fig. 4(b). In Fig. 4(c), the low interdot barrier with $\epsilon_1^{b,\rm inp} = 0.35$ was maintained, but as aforementioned, a pure intervalley-coupling term (VOC, see Sec. II D) with $\Delta = 0.05$ meV and $\phi_0 = 0$ was added to the many-body Hamiltonian $H_{\rm MB} + H_{VS}$. The red strikethrough bars over the capital letters with a "v" subscript, as well as the dashed circles over "+", 0, and "−", indicate that the valley isospin in this panel does not possess good quantum numbers due to the intervalley mixing. Nevertheless, the number of states remains unaltered and the associated topology of the spectrum in Fig. 4(c) can be traced back to that in Fig. 4(b).

For $\varepsilon > 2.8$ meV, the energy difference between the (2,0) lines indicated as e [doubly degenerate first-excited state, nos. 2,3 lines in Fig. 4(b)] and the line g [ground state, no. 1 in Fig. 4(b)] equals E_V. E_V equals also the energy difference between the middle and any outer of the three (1,1) parallel lines. The energy difference at $\varepsilon > 2.8$ between the (2,0) line indicated in Fig. 4(b) as no. 4 and the line no. 1 (ground state) equals $E^{\oplus}_{\rm ST}$. It is clear that $E^{\oplus}_{\rm ST} > E_V$ for the case illustrated in this section.

In all three panels, Figs. 4(a), 4(b), and 4(c), the three quasi-parallel lines with a large slope correspond to the (1,1) charge configuration (as indicated), whereas the quasi-horizontal lines correspond to the (2,0) charge configuration. In Fig. 4(a), where the intervalley coupling was neglected and a high barrier was applied, the avoided

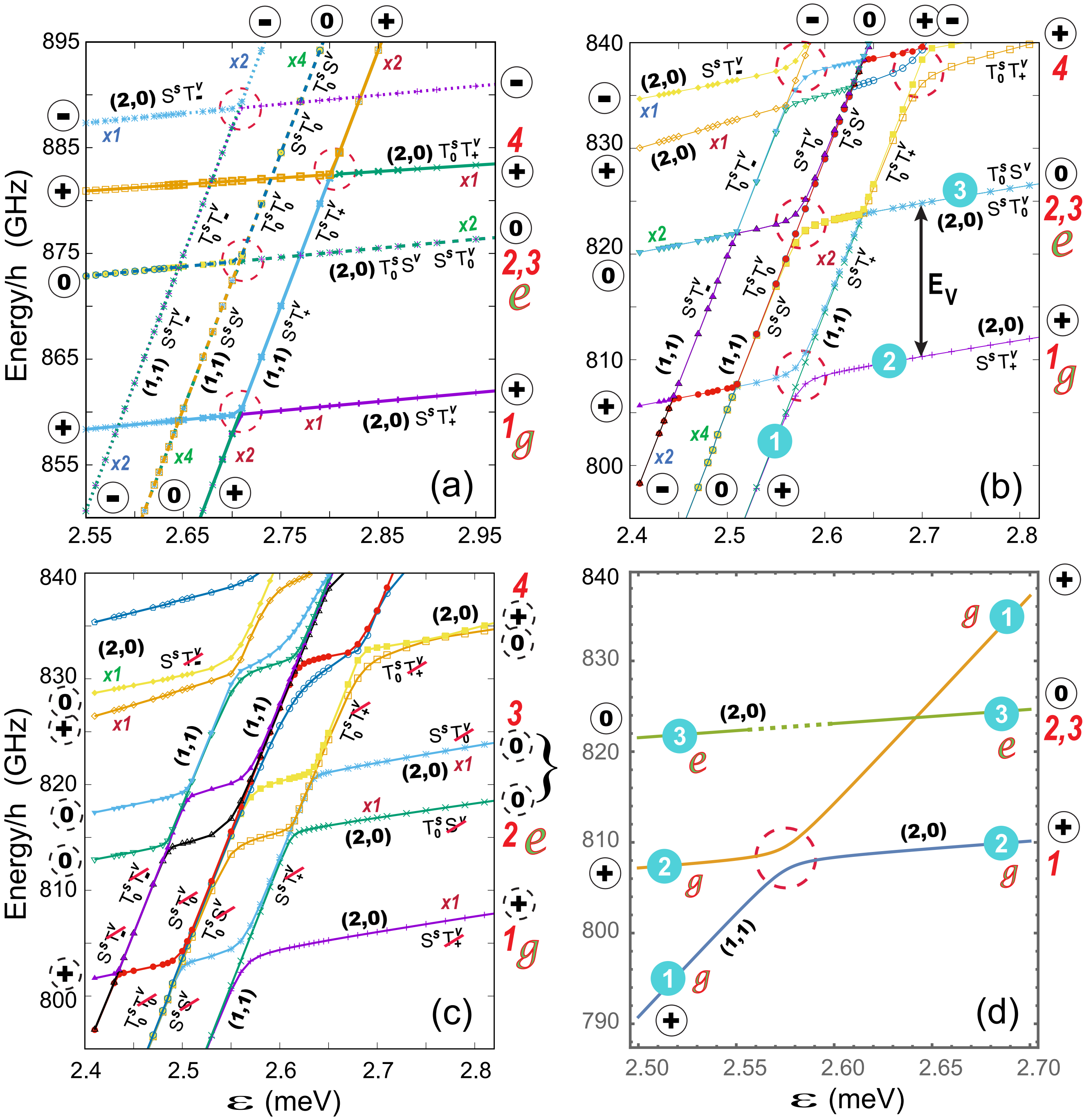

FIG. 4. The case with $E_{\rm ST}^{\oplus} > E_V$. VFCI lowest energy spectrum for the case of a Si 2e-DQD with a stronger individual-dot confinement, $\hbar\omega_0 = 0.80$ meV, for both dots, at a vanishing magnetic field, $B = 0$. The spectrum is plotted in the transition region between the (1,1) and the (2,0) charge configurations, as a function of the detuning, ε, and for a total-spin projection $S_z = 0$. The interdot separation was taken as $d = 150$ nm and the valley gap as $E_V = 60$ μeV $= 14.508h$ GHz. *The first excited state in the (2,0) configuration (state no. 2) is characterized by the symbol ⓪, that is, it has one electron in the low-energy valley and the second electron in the higher-energy valley [the script letters g and e, outside the right borders of panels (a-c) and inside panel (d), denote the ground and first-excited states in the (2,0) configuration, respectively].* (a) With a Hamiltonian $H_{\rm MB} + H_{\rm VS}$, a high interdot barrier was implemented by setting $\epsilon_1^{b,{\rm inp}} = 0.65$ (see the text for the meaning of this input barrier-controlling parameter). (b) With a Hamiltonian $H_{\rm MB} + H_{\rm VS}$, a low interdot barrier was implemented by setting $\epsilon_1^{b,{\rm inp}} = 0.35$. (c) Same as in (b), but with a $H_{\rm VOC}$ term (pure valley-orbit coupling, see text) with $\Delta = 0.05$ meV and $\phi_0 = 0$ added in the Hamiltonian. The red-strikethrough bars in panel (c), and the dashed circles outside the left and right border of that panel, indicate that the valley isospin in this panel does not possess good quantum numbers due to the intervalley mixing. (d) The three lines labeled 1, 2, and 3 on a blue disk in panel (b) reproduced according to the toy effective Hamiltonian (22). For an analysis of the trends in the spectra of this figure, see the text. The symbols $\oplus$, ⓪, and $\ominus$ have the same meaning as in Fig. 2. The in-plane Si effective mass in panels (a), (b), and (c) was taken as $0.191m_e$ and the dielectric constant as $\kappa = 11.4$.

crossings expected between curves with the same quantum numbers (see dashed circles) are very weak. Lowering the interdot barrier, however, while still neglecting intervalley coupling, yields the pronounced avoided crossings enclosed in the dashed circles of Fig. 4(b).

Introducing a non-negligible intervalley coupling in Fig. 4(c) has three effects: 1) the valley isospin is not conserved, 2) the degeneracy of states with the same valley isospin quantum numbers is lifted; see the two separate ⓪ lines (nos. 2 and 3) in Fig. 4(c) that developed out from the doubly degenerate ⓪ line (marked as "2,3") in Fig. 4(b), and 3) the pure crossings between curves with different valley quantum numbers in Fig. 4(b) transform to avoided crossings; contrast Fig. 4(b) with Fig. 4(c).

As mentioned earlier, experimental reports [31, 70] from the Wisconsin-Madison group indicated that the first excited state in the (2,0) configuration in a Si/SiGe DQD is the spin-triplet state with both electrons in the same lower-energy valley, whereas experimental measurements [28, 30] from other groups on Si-DQD devices (with apparently different parameters) indicated that the first excited energy level in this configuration is associated with a state having each electron in a different valley [see states nos. 2 or 3 in Fig. 4(b)]. In particular, using microwave-frequency scanning gate microscopy, Ref. [30] reported a measured spectrum of three lowest-energy states in the detuning window covering the transition from the (1,1) to the (2,0) configuration [98]. In Fig. 4(b), one can identify a triad of lowest-energy VFCI levels (denoted by nos. 1, 2, and 3 inside a blue disk) that have the same topology as the group of the (1,1) and the two (2,0) states in Fig. 4(b) of Ref. [30]. To further demonstrate the analogies with the experimental trends, we note that this triad of energy levels can be isolated from the full VFCI spectrum and that it can be reproduced [see Fig. 4(d)] by an effective three-level Hamiltonian as follows:

$$H_{\rm eff} = \begin{pmatrix} \alpha_1\widetilde{\varepsilon}+C & \delta & 0 \\ \delta & \alpha_2\widetilde{\varepsilon}+C & 0 \\ 0 & 0 & \alpha_3\widetilde{\varepsilon}+C+E_V \end{pmatrix}, \tag{22}$$

where $\widetilde{\varepsilon} = \varepsilon - \varepsilon_0$ with $\varepsilon_0 = 621.63h$ GHz ($= 2.575$ meV), $\alpha_1 = 0.957$, $\alpha_2 = \alpha_3 = 0.065$, $C = 808.25h$ GHz, $\delta = 1.3h$ GHz, and $E_V = 14.51h$ GHz ($= 60$ μeV), i.e., the valley splitting used in the VFCI calculation.

The interaction between the (2,0) ⊕ ground state and the (1,1) ⊕ ground state generates a visible avoided crossing, in agreement with the experiment. In contrast, using the parameters above, the (2,0) ⓪ first-excited state in Fig. 4(d) does not develop any avoided crossing with the (1,1) ⊕ ground-state curve. This is in remarkable agreement with the behavior of the experimental curves, suggesting that the valley-orbit coupling in the experimental device is either absent or rather weak.

We note that, although the value of the Wigner parameter $R_W = 7.07$ in this section is not strong enough (compared to $R_W = 10.0$ in Sec. III A) to suppress the $E_{\rm ST}^{\oplus}$ energy below E_V, the value of $E_{\rm ST}^{\oplus}$ at $\varepsilon = 2.8$ is still drastically lower than the orbital gap $\hbar\omega_0 = 0.80$ meV $= 193.44h$ GHz, i.e., at $\varepsilon = 2.95$ meV, one has $E_{\rm ST}^{\oplus} \approx 21.52h$ GHz in Fig. 4(a) and, at $\varepsilon = 2.81$ meV, $E_{\rm ST}^{\oplus} \approx 27.84h$ GHz in Fig. 4(b); for the definition of the Wigner parameter R_W, see Sec. II A.

C. Magnetic-field spectra

To further illustrate the capabilities of the present VFCI, we investigate in this section the dependence on the magnetic field, B, of the spectra of a Si 2e-DQD in the (1,1) charge configuration. For the example case here, we use an individual-dot confinement $\hbar\omega_0 = 0.40$ meV, an interdot separation $d = 150$ nm, and a valley splitting $E_V = 0.06$ meV $= 14.508h$ GHz, as was the case in Sec. III A. For the detuning, a small value of $\varepsilon = 0.05$ meV was used to guarantee that the DQD remains in the (1,1) charge configuration. The Landé factor was taken as $g^* = 2$, appropriate for silicon.

Fig. 5 displays, as a function of B, the spectra associated with the 16 low-energy states of the 2e-DQD specified in the previous paragraph. We stress again that the number 16 is a hallmark of the underlying SU(4) $\supset$ SU(2) $\times$ SU(2) symmetry-group chain, as discussed in Sec. III A 3. In particular, for comparison, Fig. 5(a) displays the 16-state spectrum in the absence of any spin-isospin coupling. Actually, considering both terms in Eq. (18), we implemented such a SIC coupling with a very small strength $\Delta = 0.00001$ meV. This small value does not generate visible avoided crossings, but it helps to enforce good spin and isospin quantum numbers by lifting the degeneracies in the spectrum by an imperceptible amount.

From Fig. 5(a), it is seen that the three original multiplets at $B = 0$ (grouped as 4 ⊕,8 ⓪, 4 ⊖) break down and fan out with increasing B. Indeed, the states with $S_z = 0$ run parallel to the B-axis, whereas states with $S_z = 1$ exhibit an ascending sloping and states with $S_z = -1$ exhibit a descending sloping. No avoided crossings are visible in Fig. 5(a), and the energy lines can be characterized by good spin and valley-isospin quantum numbers [as indicated in Fig. 5(a)].

We note that consideration of the full spin-isospin coupling requires the enlargement of the Hilbert space defined by the basis Slater determinants (see Sec. II), i.e., Slater determinants preserving individually all three values (0, ± 1) of the total spin projection, S_z, and isospin projection, V_z, must be included in the basis, and this was done for the calculations in both Figs. 5(a) and 5(b).

In contrast to Fig. 5(a), the results displayed in Fig. 5(b) correspond to an $H_{\rm SIC}$ term with a rather large strength, $\Delta = 0.03$ meV. The spin and valley isospin do not have good quantum numbers anymore, but the number of states remains unaltered and the associated topology can be traced back to that in Fig. 5(a). On the other hand, well visible avoided crossings develop in three spots (highlighted within circles) whenever the valley gap E_V equals the Zeeman energy $E_Z = g^*\mu_B B$

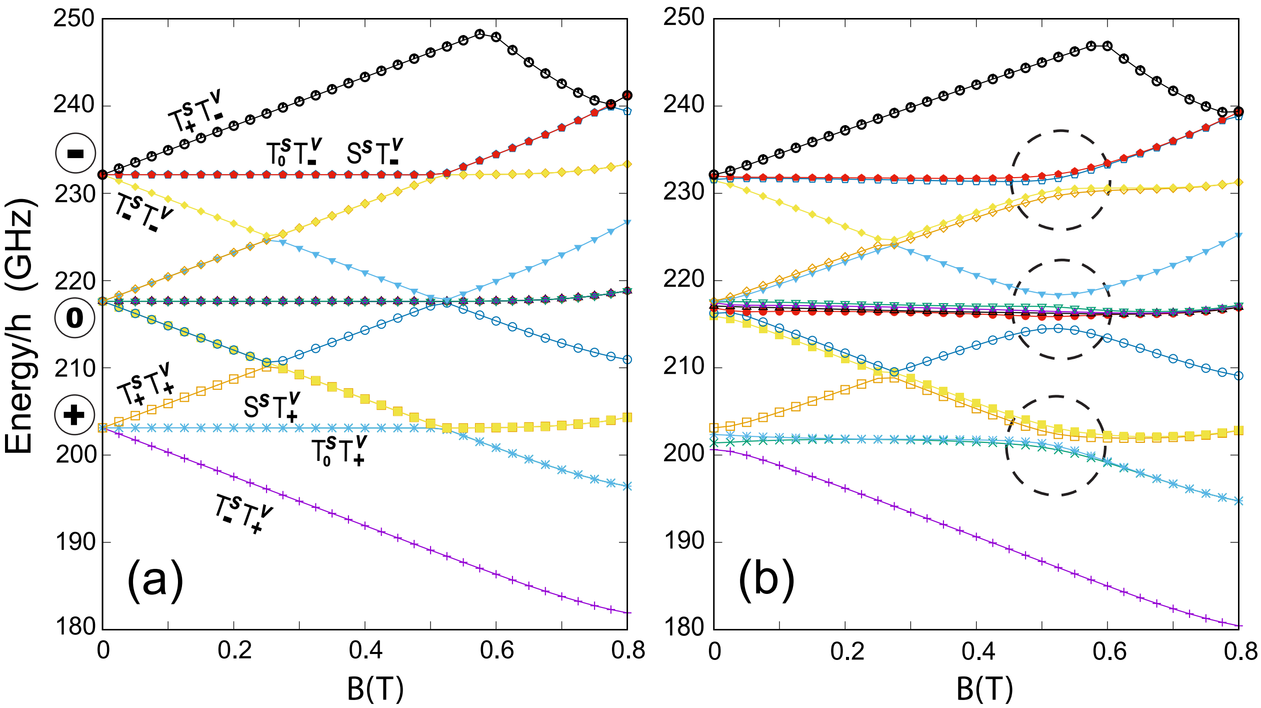

FIG. 5. VFCI spectra of the extended Hamiltonian $H_{\rm MB} + H_{\rm VS} + H_{\rm SIC}$ for the 16 low-energy states associated with the (1,1) configurations of a singlet-triplet Si 2e-DQD qubit at small detuning as a function of a perpendicular magnetic field B. $H_{\rm SIC}$ includes both contributions according to Eq. (18). (a) Case of a very small SIC coupling parameter $\Delta = 0.00001$ meV. This practically vanishing value does not generate visible avoided crossings, but it helps to enforce good spin and isospin quantum numbers by lifting the degeneracies in the spectrum by imperceptible amounts. For the $\oplus$ (both electrons in the lower-energy valley) and $\ominus$ (both electrons in the higher-energy valley) states, these quantum numbers are indicated in the figure. For the ⓪ states (one electron in each valley), these quantum numbers are as follows: $\mathrm{T}_+^s\mathrm{S}^v$ and $\mathrm{T}_+^s\mathrm{T}_0^v$ for the upper branch; $\mathrm{S}^s\mathrm{S}^v$, $\mathrm{S}^s\mathrm{T}_0^v$, $\mathrm{T}_0^s\mathrm{S}^v$, and $\mathrm{T}_0^s\mathrm{T}_0^v$ for the middle branch; $\mathrm{T}_-^s\mathrm{S}^v$ and $\mathrm{T}_-^s\mathrm{T}_0^v$ for the lower branch. These quantum numbers correspond to the VFCI results for the spin and isospin quantum numbers; for a detailed example, see Table I in Appendix B. (b) Case of a larger SIC parameter $\Delta = 0.03$ meV. The generation of avoided crossings is visible in the three encircled areas. Because of the avoided crossings brought about by the large SIC parameter, the electronic states are mixed [lose their good quantum numbers; see for comparison the labeled states for the practically vanishing Δ parameter in panel (a)]. Therefore, the labels of the states are omitted in panel (b), but the 'parentage' of the states may be inferred straightforwardly from comparisons and direct correspondences with the labeled states in panel (a). There is good overall agreement with the experimental results and phenomenological analysis in Ref. [71]. The remaining parameters for the DQD are: individual-dot confinement $\hbar\omega_0 = 0.40$ meV (for both dots), $E_V = 0.06$ meV, $\varepsilon = 0.05$ meV, $m^* = 0.191\ m_e$, $\epsilon_1^{b,\rm inp} = 0.50$, and Landé factor $g^* = 2$; see Sec. II B for the meaning of the input barrier-controlling parameter $\epsilon_1^{b,\rm inp}$.

($\mu_B = 5.788383\ 10^{-5}$ eV/Tesla is the Bohr magneton).

Our VFCI results for the case of a Si 2e-DQD portrayed in Fig. 5(b) are in agreement with the experimental results and the phenomenological analysis of Ref. [71]; see, e.g., Fig. 5(b) therein. We note further that such an avoided crossing associated with the condition $E_V = E_Z$ has been observed experimentally for other Si nanostructures, e.g., in the case of a single QD [21]. In Ref. [88], the avoided crossing at $E_V = E_Z$ was produced in a Si 2e-DQD by keeping the magnetic field constant while varying the valley splitting as a result of the application of a changing gate voltage.

IV. SUMMARY

In this paper, a valleytronic FCI has been introduced that integrates in its formalism the SU(4) ⊃ SU(2) × SU(2) group-theoretical organizational principles underlying the variety of multiplicities in the electronic spectra of a Si DQD qubit. A first application was presented concerning a detailed and complete analysis of the spectra of a 2e-DQD qubit.

In the case of the two operational low-energy valleys of a Si qubit, this was achieved by exploiting the fact that the valley degree of freedom can, to a very good approximation, be treated as an isospin [61] in complete analogy with the regular spin – as was to be intuitively expected from well-known quantum systems in other fields consisting of four species of fermions, such as atomic nuclei [64] and metal ions of many transition metal oxides [65].

Using the effective mass treatment of the low-energy valleys of Si nanodevices in conjunction with a highly adaptable TCO emulation of the artificial gate confinement in a Si DQD qubit, we have introduced an appropriate single-particle set of space orbitals, which, when augmented through multiplication with the spin and isospin up and down functions, are used as the input of spin-isospin-orbitals in the construction of the many-body CI basis of Slater determinants (Sec. II).

We demonstrated that our VFCI is able to offer a unified analysis for the spectra of a Si 2e-DQD that encompasses all three cases considered. The first two cases concerned the full spectra, including the most important avoided crossings, as a function of detuning in the transition range from the (1,1) to the (2,0) charge configuration when: (i) the formation of a strong Wigner molecule (see Fig. 2) suppresses the energy of the first-excited state, $E_{\rm ST}^{\oplus}$, within the same low-energy valley below the valley gap, E_V (Sec. III A), and (ii) in conjunction with the formation of a weaker WM, the valley gap E_V determines the energy of the first-excited state (Sec. III B). The third case concerned the evolution of the spectrum in the (1,1) configuration as a function of the magnetic field, while keeping the detuning parameter constant (Sec. III C).

When the many-body Hamiltonian accounts for the valley splitting, but does not include any valley-orbit or spin-valley coupling, the 16 hallmark (Sec. III A 3) low-energy states of the SU(4) ⊃ SU(2) × SU(2) chain are organized in multiplets according to a 4 ⊕,8 ⓪,4 ⊖ scheme for all three cases mentioned above and as long as the system remains in the (1,1) configuration, which induces spin-singlet−spin-triplet degeneracies due to the large interdot distance; for convenience we reiterate here the definitions of the symbols ⊕, ⓪, and ⊖, which indicate states with both electrons in the low-energy valley, with the electrons in different valleys, and with both electrons in the high-energy valley, respectively (see Sec. III A 1).

When the system transitions to the (2,0) charge configuration, this scheme is modified because the spin-singlet−spin-triplet degeneracies are lifted; however, the hallmark family of 16 states persists and is easily traceable in the spectra (see Figs. 2 and 4), as it fans out from the 4 ⊕,8 ⓪,4 ⊖ scheme in response to the increasing values of the detuning, ε. For the cases (i) and (ii), the enhancement of the avoided-crossing gaps in response to a reduced interdot barrier has been demonstrated explicitly [see Figs. 2(b) and 4(b)]. Furthermore, the transformation of additional simple crossings to prominent avoided ones upon consideration of a valley-orbit coupling has been discussed in Sec. III B and illustrated in Fig. 4(c).

Of particular interest are the magnetic-field-dependent VFCI spectra (third case considered, see Sec. III C), which illustrate the influence of the full SIC coupling, including a spin-valley coupling [21, 71, 88, 99, 100] which flips both the valley and spin indices. In particular, the VFCI magnetic-field spectra in the (1,1) configuration do confirm the appearance of avoided crossings [see Fig. 5(b)] at the point where the Zeeman energy, E_Z, equals the valley splitting, E_V.

As elaborated in the main text, the VFCI results presented here are in agreement with the many trends revealed in experimental measurements on actual DQD artificial devices that aim at establishing the proof-of-principle feasibility of solid-state qubits and logical gates; specifically, among others, the VFCI results were shown to emulate trends reported in Refs. [28, 30, 31, 70, 71].

In conclusion: With respect to the broader picture, the present paper takes a definitive step towards remedying the current incomplete understanding of the complexity of the spectra of Si solid-state qubits. Indeed, it has succeeded in integrating under the same framework of an efficient microscopic approach (namely the valleytronic FCI, see Sec. II C) the following pertinent aspects: 1) the valley degree of freedom as an isospin, in complete analogy with the regular spin, 2) the SU(4) ⊃ SU(2) × SU(2) group-theoretical organization of the spectra, containing the salient features of avoided crossings, 3) the effect of strong $e-e$ correlations and of the ensuing formation of WMs in the experimentally relevant context of realistic double-well confining potentials, which strongly suppresses the spin-singlet−spin-triplet gaps within the same valley, and 4) the influence of valley-orbit and spin-valley Hamiltonian terms, in particular under an applied magnetic field.

This valleytronic FCI, demonstrated for the case of two electrons confined in a tunable double quantum dot, offers also a most effective tool for analyzing the spectra of Si qubits with more than two wells and/or more than two electrons under field-free conditions and in the presence of a magnetic field. Moreover, this methodology can be readily adapted and employed for treatment of the many-body problem in diverse model devices, with carriers (electrons or holes in semi-conductors, e.g. Si or Ge) confined in dots of variable sizes and symmetries, e.g. two-dimensional (circular, elliptical), or quasi-one-dimensional elongated structures (wire-like [11, 14, 16]), or like the one presented most recently in Ref. [101], as well as be extended [102] to treat the case of bilayer graphene quantum dots [72, 73].

Appendix A: Solving the auxiliary Hamiltonian eigenvalue problem

For a given interwell separation d, the spatial orbitals $\varphi_i(\mathbf{r})$, $i = 1, \ldots, K$ that form the single-particle basis [see Eq. (9)] are obtained by a semi-analytic diagonalization of the auxiliary single-particle Hamiltonian specified in Eq. (8).

Specifically, the eigenvalue problem associated with the auxiliary Hamiltonian [Eq. (8)] is separable in the x and

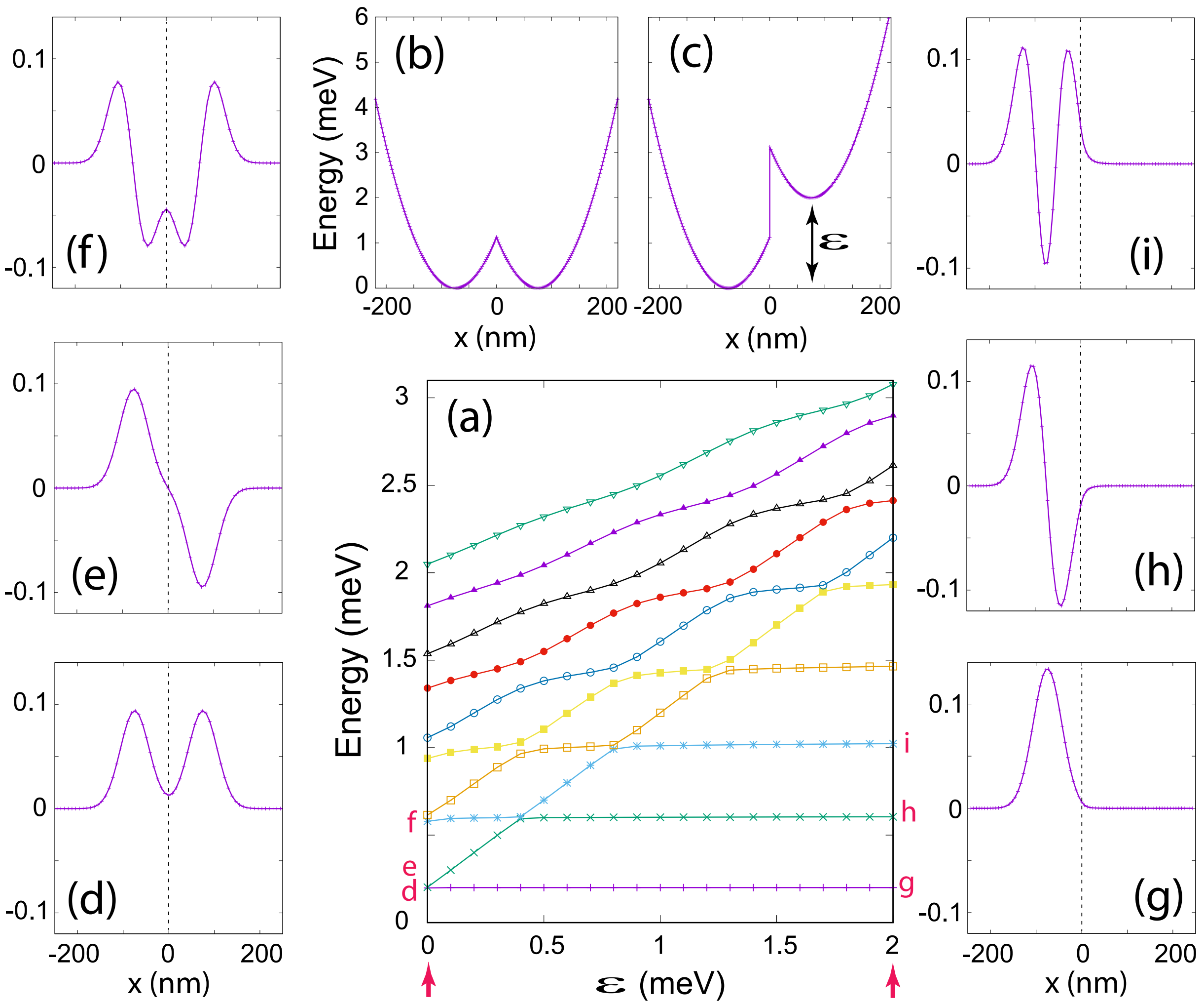

FIG. 6. Illustration of the single-particle basis. (a) Energies, as a function of the detuning ε, of the first ten states of the one-dimensional Hamiltonian $H^{(x)}_{\rm aux}$ [see Eq. (A1)] that participate in the single-particle basis associated with the 2D Hamiltonian $H_{\rm aux}$. Frames (b) and (c) display the corresponding potential confinements, $m^*\omega^2_{xk}x'^2_k/2 + h_k$, at two values of the detuning (indicated by the two upwards-pointing arrows), i.e, at $\varepsilon = 0$ and $\varepsilon = 2.0$ meV, respectively; here $h_1 = 0$ and $h_2 = \varepsilon$. The associated single-particle wave functions $X_{\mu(j)}(x)$ for $j = 1, \ldots, 3$ [see Eq. (A2)] are also displayed at these two points; see panels (d-f) for $\varepsilon = 0$ and panels (g-i) for $\varepsilon = 2.0$ meV. We mention that the smooth-neck Hamiltonian term, $V_{\rm neck}(x)$, is not included in $H_{\rm aux}$. The parameters entering in $H^{(x)}_{\rm aux}$ were chosen as: confinement $\hbar\omega_{x1} = \hbar\omega_{x2} = \hbar\omega_0 = 0.40$ meV, interwell distance $d = 150$ nm (with $-x_1 = x_2 = 75$ nm), and effective mass $m^* = 0.191 m_e$ (appropriate for Si). The wave functions in the panels (d-f) and (g-i) are in units of $1/\sqrt{nm}$.

y variables, i.e., one has

$$H_{\rm aux} = H^{(x)}_{\rm aux} + H^{(y)}_{\rm aux}, \tag{A1}$$

and as a result the single-particle wave functions are written as

$$\varphi_j(x, y) = X_\mu(x)Y_n(y), \tag{A2}$$

with $j \equiv \{\mu, n\}$, $j = 1, 2, \ldots, K$. As mentioned earlier, K specifies the size of the single-particle basis.

The $Y_n(y)$ are the eigenfunctions of a one-dimensional oscillator in the y direction, and the $X_\mu(x \leq 0)$ and $X_\mu(x > 0)$ can be expressed through the parabolic cylinder functions $U[\gamma_k, (-1)^k\xi_k]$ [103], where $\xi_k = x'_k\sqrt{2m^*\omega_{xk}/\hbar}$, $\gamma_k = (-E_x + h_k)/(\hbar\omega_{xk})$, and $E_x = (\mu+0.5)\hbar\omega_{x1}+h_1$ denotes the x-eigenvalues. The matching conditions at $x = 0$ for the left ($k = 1$) and right ($k = 2$) domains yield the x-eigenvalues and the eigenfunctions $X_\mu(x)$. The n indices are integer numbers. The μ indices are in general real numbers, but their number is finite.

An advantage of the single-particle orbital basis described in this section is the fact that it adapts continuously to both the interwell separation d and the detuning parameter ε. As a result, a very efficient convergence is achieved for any d and ε. The adaptability of our single-particle orbital basis is illustrated in Fig. 6. In particular,

TABLE I. The VFCI calculated expectation values $\langle \ldots \rangle$ for the total spin and total isospin associated with the VFCI states in Fig. 5(a) at a magnetic-field value of $B = 0.05$ T. The 16 displayed states are labeled in this Table in ascending energy-eigenvalue order, with the ground state being labeled as no. 1. Deviations from the expected group-theoretical values, i.e., $\langle \hat{\mathbf{S}}^2 \rangle_{\rm exact} = \mathcal{S}(\mathcal{S}+1)$ and $\langle \hat{\mathbf{V}}^2 \rangle_{\rm exact} = \mathcal{V}(\mathcal{V}+1)$ (0 or 2), and $\langle S_z \rangle_{\rm exact} = 0, \pm 1$, $\langle V_z \rangle_{\rm exact} = 0, \pm 1$, appear at most at the fifth decimal point. The symbols ⊕, ⓪, and ⊖ have the same meaning as in Fig. 2.

	Energy/h (GHz)	$\langle \hat{\mathbf{S}}^2 \rangle$	$\langle \hat{\mathbf{V}}^2 \rangle$	$\langle S_z \rangle$	$\langle V_z \rangle$	
1	201.722160	2.00000	2.00000	-1.0000	1.0000	⊕
2	203.121755	0.00000	2.00000	-0.0000	1.0000	⊕
3	203.121774	2.00000	2.00000	-0.0000	1.0000	⊕
4	204.521388	2.00000	2.00000	1.0000	1.0000	⊕
5	216.229963	2.00000	0.00001	-1.0000	0.0000	⓪
6	216.229983	2.00000	1.99999	-1.0000	0.0000	⓪
7	217.629577	0.00000	1.99999	-0.0000	0.0000	⓪
8	217.629577	2.00000	0.00001	-0.0000	0.0000	⓪
9	217.629596	0.00000	0.00001	-0.0000	0.0000	⓪
10	217.629596	2.00000	1.99999	-0.0000	0.0000	⓪
11	219.029191	2.00000	0.00001	1.0000	-0.0000	⓪
12	219.029210	2.00000	1.99999	1.0000	-0.0000	⓪
13	230.737805	2.00000	2.00000	-1.0000	-1.0000	⊖
14	232.137399	0.00000	2.00000	0.0000	-1.0000	⊖
15	232.137419	2.00000	2.00000	0.0000	-1.0000	⊖
16	233.537032	2.00000	2.00000	1.0000	-1.0000	⊖

Fig. 6(a) displays eigenvalues of the non-trivial auxiliary Hamiltonian $H_{\rm aux}^{(x)}$ [see Eq. (A1)] which implements the TCO confinement along the x direction. One observes that for larger values of detuning, these eigenvalues become constant (as was to be expected), and they run parallel to the ε axis.

Two cases of the TCO potential confinement are also displayed in Figs. 6(b) and 6(c), the former corresponding to a symmetric double well ($\varepsilon = 0$) and the latter to the case when the right well is strongly higher by $\varepsilon = 2.0$ meV. The corresponding three lowest-energy eigenfunctions are also displayed in the triad of Figs. 6(d-f) and the triad of Figs. 6(g-i) for these two values of ε, respectively. It is seen that the eigenfunctions in Figs. 6(d-f) preserve the parity around the origin and extend over both wells (as was to be expected for a symmetric double well), whereas those in Figs. 6(g-i) are restricted within the left well (as was to be expected again for a highly tilted double well) [104].

We mention again that the smooth-neck Hamiltonian term, $V_{\rm neck}(x)$, is not included in $H_{\rm aux}$.

The contributions in the many-body Hamiltonian from the smooth-neck term, the magnetic-field-dependent terms, and the spin- and isospin-dependent terms are calculated as part of the many-body exact diagonalization by using the Slater-Condon rules for one-body operators between pairs of the Slater determinants Ψ_I^N [see Eq. (11)].

Appendix B: An example of VFCI results concerning the spin and isospin quantum numbers

In this Appendix, we give an example (see Table I) of VFCI calculated expectation values that correspond to complete sets of the four integer quantum numbers that are expected from group theoretical considerations for the total spin and the total valley isospin. Deviations from the appropriate integer values, if any, appear at most at the fifth decimal digit.

[1] F. A. Zwanenburg, A. S. Dzurak, A. Morello, M. Y. Simmons, L. C. L. Hollenberg, G. Klimeck, S. Rogge, S. N. Coppersmith, and M. A. Eriksson, Silicon quantum electronics, Rev. Mod. Phys. **85**, 961–1019 (2013).

[2] L. M. K. Vandersypen and M. A. Eriksson, Quantum computing with semiconductor spins, Phys. Today **72**, 38–45 (2019).

[3] G. Burkard, T. D. Ladd, J. M. Nichol, A. Pan, and J. R. Petta, Semiconductor Spin Qubits, arXiv:2112.08863.

[4] A. Chatterjee, P. Stevenson, S. De Franceschi, A. Morello, N. P. de Leon, and F. Kuemmeth, Semiconductor qubits in practice, Nature Reviews Physics **3**, 157–177 (2021).

[5] X. Xue, M. Russ, N. Samkharadze, B. Undseth, A. Sammak, G. Scappucci, and L. M. K. Vandersypen, Quantum logic with spin qubits crossing the surface code threshold, Nature **601**, 343–347 (2022).

[6] A. Noiri, K. Takeda, T. Nakajima, T. Kobayashi, A. Sammak, G. Scappucci, and S. Tarucha, Fast universal quantum gate above the fault-tolerance threshold in silicon, Nature **601**, 338–342 (2022).

[7] A. J. Weinstein, M. D. Reed, A. M. Jones, R. W. Andrews, D. Barnes, J. Z. Blumoff, L. E. Euliss, K. Eng, B. Fong, S. D. Ha, D. R. Hulbert, C. Jackson, M. Jura, T. E. Keating, J. Kerckhoff, A. A. Kiselev, J. Matten, G. Sabbir, A. Smith, J. Wright, M. T. Rakher, T. D. Ladd, and M. G. Borselli, Universal logic with encoded spin qubits in silicon, arxiv:2202.03605.

[8] J. R. Petta, A. C. Johnson, J. M. Taylor, E. A. Laird, A. Yacoby, M. D. Lukin, C. M. Marcus, M. P. Hanson, and A. C. Gossard, Coherent manipulation of coupled electron spins in semiconductor quantum dots, Science **309**, 2180–2184 (2005).

[9] W. Jang, M.-K. Cho, H. Jang, J. Kim, J. Park, G. Kim, B. Kang, H. Jung, V. Umansky, and D. Kim, Single-Shot Readout of a Driven Hybrid Qubit in a GaAs Double Quantum Dot, Nano Letters **21**, 4999–5005 (2021).

[10] W. Jang, J. Kim, J. Park, G. Kim, M.-K. Cho, H. Jang, S. Sim, B. Kang, H. Jung, V. Umansky, and D. Kim, Wigner-molecularization-enabled dynamic nuclear field programming, arXiv:2207.11655.

[11] R. Maurand, X. Jehl, D. Kotekar-Patil, A. Corna, H. Bohuslavskyi, R. Laviéville, L. Hutin, S. Barraud, M. Vinet, M. Sanquer, and S. De Franceschi, A CMOS silicon spin qubit, Nature Communications **7**, 13575 (2016).

[12] J. C. Abadillo-Uriel, B. Martinez, M. Filippone, and Y.-M. Niquet, Two-body Wigner molecularization in asymmetric quantum dot spin qubits, Phys. Rev. B **104**, 195305 (2021).

[13] L. A. Terrazos, E. Marcellina, Z. Wang, S. N. Coppersmith, M. Friesen, A. R. Hamilton, X. Hu, B. Koiller, A. L. Saraiva, D. Culcer, and R. B. Capaz, Theory of hole-spin qubits in strained germanium quantum dots, Phys. Rev. B **103**, 125201 (2021).

[14] F. N. M. Froning, L. C. Camenzind, O. A. H. van der Molen, A. Li, E. P. A. M. Bakkers, D. M. Zumbühl, and F. R. Braakman, Ultrafast hole spin qubit with gate-tunable spin–orbit switch functionality, Nature Nanotechnology **16**, 308–312 (2021).

[15] D. Jirovec, P. M. Mutter, A. Hofmann, A. Crippa, M. Rychetsky, D. L. Craig, J. Kukucka, F. Martins, A. Ballabio, N. Ares, D. Chrastina, G. Isella, G. Burkard, and G. Katsaros, Dynamics of hole singlet-triplet qubits with large g-factor differences, Phys. Rev. Lett. **128**, 126803 (2022).

[16] K. Wang, G. Xu, F. Gao, H. Liu, R.-L. Ma, X. Zhang, Z. Wang, G. Cao, T. Wang, J.-J. Zhang, D. Culcer, X. Hu, H.-W. Jiang, H.-O. Li, G.-C. Guo, and G.-P. Guo, Ultrafast coherent control of a hole spin qubit in a germanium quantum dot, Nature Communications **13**, 206 (2022).

[17] G. Scappucci, C. Kloeffel, F. A. Zwanenburg, D. Loss, M. Myronov, J.-J. Zhang, S. De Franceschi, G. Katsaros, and M. Veldhorst, The germanium quantum information route, Nature Reviews Materials **6**, 926–943 (2021).

[18] C. Ellenberger, T. Ihn, C. Yannouleas, U. Landman, K. Ensslin, D. Driscoll, and A. C. Gossard, Excitation Spectrum of Two Correlated Electrons in a Lateral Quantum Dot with Negligible Zeeman Splitting, Phys. Rev. Lett. **96**, 126806 (2006).

[19] D. Culcer, L. Cywiński, Q. Li, X. Hu, and S. Das Sarma, Quantum dot spin qubits in silicon: Multivalley physics, Phys. Rev. B **82**, 155312 (2010).

[20] B. M. Maune, M. G. Borselli, B. Huang, T. D. Ladd, P. W. Deelman, K. S. Holabird, A. A. Kiselev, I. Alvarado-Rodriguez, R. S. Ross, A. E. Schmitz, M. Sokolich, C. A. Watson, M. F. Gyure, and A. T. Hunter, Coherent singlet-triplet oscillations in a silicon-based double quantum dot, Nature **481**, 344–347 (2012).

[21] C. H. Yang, A. Rossi, R. Ruskov, N. S. Lai, F. A. Mohiyaddin, S. Lee, C. Tahan, G. Klimeck, A. Morello, and A. S. Dzurak, Spin-valley lifetimes in a silicon quantum dot with tunable valley splitting, Nature Communications **4**, 2069 (2013).

[22] E. Kawakami, P. Scarlino, D. R. Ward, F. R. Braakman, D. E. Savage, M. G. Lagally, M. Friesen, S. N. Coppersmith, M. A. Eriksson, and L. M. K. Vandersypen, Electrical control of a long-lived spin qubit in a Si/SiGe quantum dot, Nature Nanotechnology **9**, 666–670 (2014).

[23] G. Burkard and J. R. Petta, Dispersive readout of valley splittings in cavity-coupled silicon quantum dots, Phys. Rev. B **94**, 195305 (2016).

[24] R. Ruskov, M. Veldhorst, A. S. Dzurak, and C. Tahan, Electron g-factor of valley states in realistic silicon quantum dots, Phys. Rev. B **98**, 245424 (2018).

[25] X. Mi, S. Kohler, and J. R. Petta, Landau-Zener interferometry of valley-orbit states in Si/SiGe double quantum dots, Phys. Rev. B **98**, 161404 (2018).

[26] R. C. C. Leon, C. H. Yang, J. C. C. Hwang, J. C. Lemyre, T. Tanttu, W. Huang, K. W. Chan, K. Y. Tan, F. E. Hudson, K. M. Itoh, A. Morello, A. Laucht, M. Pioro-Ladrière, A. Saraiva, and A. S. Dzurak, Coherent spin control of s-, p-, d- and f-electrons in a silicon quantum dot, Nature Communications **11**, 797 (2020).

[27] T. McJunkin, B. Harpt, Y. Feng, M. Losert, R. Rahman, J. P. Dodson, M. A. Wolfe, D. E. Savage, M. G. Lagally, S. N. Coppersmith, M. Friesen, R. Joynt, and M. A. Eriksson, SiGe quantum wells with oscillating Ge concentrations for quantum dot qubits, arXiv:2112.09765.

[28] X. Cai, E. J. Connors, and J. M. Nichol, Coherent spin-valley oscillations in silicon, arXiv:2111.14847.

[29] H. E. Ercan, M. Friesen, and S. N. Coppersmith, Charge-Noise Resilience of Two-Electron Quantum Dots in Si/SiGe Heterostructures, Phys. Rev. Lett. **128**, 247701 (2022).

[30] A. O. Denisov, S. W. Oh, G. Fuchs, A. R. Mills, P. Chen, C. R. Anderson, M. F. Gyure, A. W. Barnard, and J. R. Petta, Microwave-frequency scanning gate microscopy of a Si/SiGe double quantum dot, arXiv:2203.05912.

[31] J. Corrigan, J. P. Dodson, H. E. Ercan, J. C. Abadillo-Uriel, B. Thorgrimsson, T. J. Knapp, N. Holman, T. McJunkin, S. F. Neyens, E. R. MacQuarrie, R. H. Foote, L. F. Edge, M. Friesen, S. N. Coppersmith, and M. A. Eriksson, Coherent Control and Spectroscopy of a Semiconductor Quantum Dot Wigner Molecule, Phys. Rev. Lett. **127**, 127701 (2021).

[32] H. E. Ercan, S. N. Coppersmith, and M. Friesen, Strong electron-electron interactions in Si/SiGe quantum dots, Phys. Rev. B **104**, 235302 (2021).

[33] J. Corrigan *et al.*, arXiv:2009.13572v1.

[34] C. Yannouleas and U. Landman, Spontaneous Symmetry Breaking in Single and Molecular Quantum Dots, Phys. Rev. Lett. **82**, 5325–5328 (1999).

[35] R. Egger, W. Häusler, C. H. Mak, and H. Grabert, Crossover from Fermi Liquid to Wigner Molecule Behavior in Quantum Dots, Phys. Rev. Lett. **82**, 3320–3323 (1999).

[36] C. Yannouleas and U. Landman, Collective and Independent-Particle Motion in Two-Electron Artificial Atoms, Phys. Rev. Lett. **85**, 1726–1729 (2000).

[37] C. Yannouleas and U. Landman, Formation and control of electron molecules in artificial atoms: Impurity and magnetic-field effects, Phys. Rev. B **61**, 15895–15904 (2000).

[38] A. V. Filinov, M. Bonitz, and Y. E. Lozovik, Wigner Crystallization in Mesoscopic 2D Electron Systems, Phys. Rev. Lett. **86**, 3851–3854 (2001).

[39] C. Yannouleas and U. Landman, Magnetic-field manipulation of chemical bonding in artificial molecules, International Journal of Quantum Chemistry **90**, 699–708 (2002).

[40] C. Yannouleas and U. Landman, Strongly correlated wavefunctions for artificial atoms and molecules, Journal of Physics: Condensed Matter **14**, L591–L598 (2002).

[41] M. B. Tavernier, E. Anisimovas, F. M. Peeters, B. Szafran, J. Adamowski, and S. Bednarek, Four-electron quantum dot in a magnetic field, Phys. Rev. B **68**, 205305 (2003).

[42] M. Rontani, C. Cavazzoni, D. Bellucci, and G. Goldoni, Full configuration interaction approach to the few-electron problem in artificial atoms, The Journal of Chemical Physics **124**, 124102 (2006).

[43] Y. Li, C. Yannouleas, and U. Landman, Three-electron anisotropic quantum dots in variable magnetic fields: Exact results for excitation spectra, spin structures, and entanglement, Phys. Rev. B **76**, 245310 (2007).

[44] C. Yannouleas and U. Landman, Symmetry breaking and quantum correlations in finite systems: Studies of quantum dots and ultracold Bose gases and related nuclear and chemical methods, Reports on Progress in Physics **70**, 2067–2148 (2007).

[45] Y. Li, C. Yannouleas, and U. Landman, Artificial quantum-dot helium molecules: Electronic spectra, spin structures, and Heisenberg clusters, Phys. Rev. B **80**, 045326 (2009).

[46] C. Yannouleas and U. Landman, Wigner molecules and hybrid qubits, J. Phys.: Condens. Matter (Letter) **34**, 21LT01 (2022).

[47] C. Yannouleas and U. Landman, Molecular formations and spectra due to electron correlations in three-electron hybrid double-well qubits, Phys. Rev. B **105**, 205302 (2022).

[48] C. Yannouleas and U. Landman, Two-dimensional quantum dots in high magnetic fields: Rotating-electron-molecule versus composite-fermion approach, Phys. Rev. B **68**, 035326 (2003).

[49] L. O. Baksmaty, C. Yannouleas, and U. Landman, Rapidly rotating boson molecules with long- or short-range repulsion: An exact diagonalization study, Phys. Rev. A **75**, 023620 (2007).

[50] B. B. Brandt, C. Yannouleas, and U. Landman, Double-well ultracold-fermions computational microscopy: Wave-function anatomy of attractive-pairing and wigner-molecule entanglement and natural orbitals, Nano Letters **15**, 7105–7111 (2015).

[51] C. Yannouleas, B. B. Brandt, and U. Landman, Ultracold few fermionic atoms in needle-shaped double wells: spin chains and resonating spin clusters from microscopic Hamiltonians emulated via antiferromagnetic Heisenberg and $t-J$ models, New Journal of Physics **18**, 073018 (2016).

[52] C. Yannouleas and U. Landman, Electron and boson clusters in confined geometries: Symmetry breaking in quantum dots and harmonic traps, Proceedings of the National Academy of Sciences **103**, 10600–10605 (2006).

[53] C. Yannouleas and U. Landman, Exact closed-form analytic wave functions in two dimensions: Contact-interacting fermionic spinful ultracold atoms in a rapidly rotating trap, Phys. Rev. Research **3**, L032028 (2021).

[54] I. Shavitt, The history and evolution of configuration interaction, Molecular Physics **94**, 3–17 (1998).

[55] B. Joecker, A. D. Baczewski, J. K. Gamble, J. J. Pla, A. Saraiva, and A. Morello, Full configuration interaction simulations of exchange-coupled donors in silicon using multi-valley effective mass theory, New Journal of Physics **23**, 073007 (2021).

[56] A. Rycerz, J. Tworzydło, and C. W. J. Beenakker, Valley filter and valley valve in graphene, Nature Physics **3**, 172–175 (2007).

[57] C. W. J. Beenakker, Colloquium: Andreev reflection and klein tunneling in graphene, Rev. Mod. Phys. **80**, 1337–1354 (2008).

[58] S. N. Shevchenko, A. I. Ryzhov, and F. Nori, Low-frequency spectroscopy for quantum multilevel systems, Phys. Rev. B **98**, 195434 (2018).

[59] G. Scuri, T. I. Andersen, Y. Zhou, D. S. Wild, J. Sung, R. J. Gelly, D. Bérubé, H. Heo, L. Shao, A. Y. Joe, A. M. Mier Valdivia, T. Taniguchi, K. Watanabe, M. Lončar, P. Kim, M. D. Lukin, and H. Park, Electrically Tunable Valley Dynamics in Twisted $\mathrm{WSe_2/WSe_2}$ Bilayers, Phys. Rev. Lett. **124**, 217403 (2020).

[60] M. S. Mrudul, Álvaro Jiménez-Galán, M. Ivanov, and G. Dixit, Light-induced valleytronics in pristine graphene, Optica **8**, 422–427 (2021).

[61] V. Heine, *Group Theory in Quantum Mechanics: An Introduction to Its Present Usage* (Pergamon Press, London, 1970).

[62] J. M. Luttinger and W. Kohn, Motion of electrons and holes in perturbed periodic fields, Phys. Rev. **97**, 869–883 (1955).

[63] For the application of the effective mass theory to the band structure of single carbon-nanotube QDs, see Ref. [67](b) and (a) A. Secchi and M. Rontani, Wigner molecules in carbon-nanotube quantum dots, Phys. Rev. B **82**, 035417 (2010); for the application of the effective mass theory to the band structure of single graphene QDs, see Ref. [67](a) and (b) K. A. Guerrero-Becerra and M. Rontani, Wigner localization in a graphene quantum dot with a mass gap, Phys. Rev. B **90**, 125446 (2014); for the application of the effective mass theory to the band structure of Si QDs, see (c) Y. Hada and M. Eto, Electronic states in silicon quantum dots: Multivalley artificial atoms, Phys. Rev. B **68**, 155322 (2003); (d) M. Friesen, S. Chutia, C. Tahan, and S. N. Coppersmith, Valley splitting theory of Si/SiGe quantum wells, Phys. Rev. B **75**, 115318 (2007); and (e) M. Friesen and S. N. Coppersmith, Theory of valley-orbit coupling in a Si/SiGe quantum dot, Phys. Rev. B **81**, 115324 (2010).

[64] For the earliest application of the SU(4) group theory to physics (specifically nuclear physics, based on the approximate proton-neutron equivalence), and for further original references related to the concept of the isospin (referred to also as isotopic spin), see E. Wigner, On the consequences of the symmetry of the nuclear Hamiltonian on the spectroscopy of nuclei, Phys. Rev. **51**, 106–119 (1937).

[65] For an earlier application of the SU(4) group theory to condensed-matter spin-lattice models with Hamiltonians of a generalized Heisenberg type that take into account the orbital degeneracy present in the metal ions of many transition metal oxides, see (a) Y. Q. Li, M. Ma, D. N. Shi, and F. C. Zhang, SU(4) Theory for Spin Systems with Orbital Degeneracy, Phys. Rev. Lett. **81**, 3527–3530 (1998), and references therein. See also (b) D. P. Arovas and A. Auerbach, Tetrakis(dimethylamino)ethylene-$\mathrm{C_{60}}$: Multicomponent superexchange and Mott ferromagnetism, Phys. Rev. B **52**, 10114–10121 (1995).

[66] For Hubbard-type applications of the SU(N) group theory to ultracold-atom optical lattices, see (a) S. Capponi, P. Lecheminant, and K. Totsuka, Phases of one-dimensional SU(N) cold atomic Fermi gases—from molecular Luttinger liquids to topological phases, Annals of Physics **367**, 50–95 (2016), and references therein. See also (b) C. Honerkamp and W. Hofstetter, Ultracold Fermions and the SU(N) Hubbard Model, Phys. Rev. Lett. **92**, 170403 (2004).

[67] For bilayer graphene QDs, see (a) M. Zarenia, B. Partoens, T. Chakraborty, and F. M. Peeters, Electron-electron interactions in bilayer graphene quantum dots, Phys. Rev. B **88**, 245432 (2013); for carbon nanotube QDs, see, e.g., (b) M. Roy and P. A. Maksym, Effective mass theory of interacting electron states in semiconducting carbon nanotube quantum dots, Phys. Rev. B **85**, 205432 (2012).

[68] Also CI implementations (see, e.g., Ref. [32]) for Si/SiGe single QDs that employ lattice tight-binding single-particle bases, as well as CI simulations of exchange-coupled donors in silicon using multi-valley effective mass theory [55], are using the regular spin indices $(\mathcal{S}, S_z)$ only.

[69] The notation (n_L, n_R) indicates charge configurations with n_L electrons in the left dot, and n_R electrons in the right dot.

[70] J. P. Dodson, H. E. Ercan, J. Corrigan, M. P. Losert, N. Holman, T. McJunkin, L. F. Edge, M. Friesen, S. N. Coppersmith, and M. A. Eriksson, How Valley-Orbit States in Silicon Quantum Dots Probe Quantum Well Interfaces, Phys. Rev. Lett. **128**, 146802 (2022).

[71] X. Hao, R. Ruskov, M. Xiao, C. Tahan, and H. Jiang, Electron spin resonance and spin-valley physics in a silicon double quantum dot, Nature Communications **5**, 3860 (2014).

[72] A. Kurzmann, M. Eich, H. Overweg, M. Mangold, F. Herman, P. Rickhaus, R. Pisoni, Y. Lee, R. Garreis, C. Tong, K. Watanabe, T. Taniguchi, K. Ensslin, and T. Ihn, Excited States in Bilayer Graphene Quantum Dots, Phys. Rev. Lett. **123**, 026803 (2019).

[73] S. Möller, L. Banszerus, A. Knothe, C. Steiner, E. Icking, S. Trellenkamp, F. Lentz, K. Watanabe, T. Taniguchi, L. I. Glazman, V. I. Fal'ko, C. Volk, and C. Stampfer, Probing Two-Electron Multiplets in Bilayer Graphene Quantum Dots, Phys. Rev. Lett. **127**, 256802 (2021).

[74] M. Russ and G. Burkard, Three-electron spin qubits, Journal of Physics: Condensed Matter **29**, 393001 (2017).

[75] M. L. Cohen and J. R. Chelikowsky, *Electronic Structure and Optical Properties of Semiconductors* (Springer-Verlag, Berlin, 1988).

[76] P. Y. Yu and M. Cardona, *Fundamentals of Semiconductors* (Springer-Verlag, Berlin, 2001) 3rd ed.

[77] J. C. Phillips, Band structure of Silicon, Germanium, and related semiconductors, Phys. Rev. **125**, 1931–1936 (1962).

[78] F. Schäffler, High-mobility Si and Ge structures, Semiconductor Science and Technology **12**, 1515–1549 (1997).

[79] T. Ando, A. B. Fowler, and F. Stern, Electronic properties of two-dimensional systems, Rev. Mod. Phys. **54**, 437–672 (1982).

[80] These confinement-induced single-particle energy states are also referred to as "orbitals", see, e.g., the expressions "atomic orbitals", "space orbitals", and "spin-orbitals" in chemistry [84].

[81] This is an apparent generalization of the term spin-orbital used in chemistry and molecular physics [80].

[82] See Ref. [32]; (a), (b), and (c) in Ref. [63]; (a) and (b) in Ref. [67].

[83] R. B. Lehoucq, D. C. Sorensen, and C. Yang, *ARPACK USERS' GUIDE: Solution of Large-Scale Eigenvalue Problems with Implicitly Restarted ARNOLDI Methods* (SIAM, Philadelphia, 1998).

[84] A. Szabo and N. S. Ostlund, *Modern Quantum Chemistry* (McGraw-Hill, New York, 1989) For the Slater-Condon rules, see Chap. 4.

[85] J. C. Slater, The theory of complex spectra, Phys. Rev. **34**, 1293–1322 (1929).

[86] E. U. Condon, The Theory of Complex Spectra, Phys. Rev. **36**, 1121–1133 (1930).

[87] R. Pauncz, *The Construction of Spin Eigenfunctions: An Exercise Book* (Kluwer Academic/Plenum Publishers, New York, 2000).

[88] J. C. C. Hwang, C. H. Yang, M. Veldhorst, N. Hendrickx, M. A. Fogarty, W. Huang, F. E. Hudson, A. Morello, and A. S. Dzurak, Impact of g-factors and valleys on spin qubits in a silicon double quantum dot, Phys. Rev. B **96**, 045302 (2017).

[89] The Kronecker delta explicitly couples space orbitals with different indices and thus it implements a simplification of the effect from the space derivatives present in $\widehat{O}(x, y)$ according to the original expression for the spin-orbit coupling suggested in Yu. A. Bychkov and E. I. Rashba, JETP Lett. **39**, 78 (1984).

[90] C. L. Kane and E. J. Mele, Quantum Spin Hall Effect in Graphene, Phys. Rev. Lett. **95**, 226801 (2005).

[91] The dots in all instances in this paper are placed at equal distances from the origin.

[92] A spin singlet has eigenvalues $\mathcal{S}(\mathcal{S}+1) = 0$ and $S_z = 0$, whereas a spin triplet has eigenvalues $\mathcal{S}(\mathcal{S}+1) = 2$ and $S_z = 0$ or $S_z = \pm 1$. Correspondingly, an isospin singlet has eigenvalues $\mathcal{V}(\mathcal{V}+1) = 0$ and $V_z = 0$, whereas an isospin triplet has eigenvalues $\mathcal{V}(\mathcal{V}+1) = 2$ and $V_z = 0$ or $V_z = \pm 1$.

[93] C. Yannouleas and U. Landman, Coupling and dissociation in artificial molecules, The European Physical Journal D - Atomic, Molecular, Optical and Plasma Physics **16**, 373–380 (2001).

[94] We have indeed checked the accuracy of this statement for a single elliptic Si QD using the VFCI code.

[95] L. Sárkány, E. Szirmai, C. P. Moca, L. Glazman, and G. Zaránd, Wigner crystal phases in confined carbon nanotubes, Phys. Rev. B **95**, 115433 (2017).

[96] An additional multiplet of 10 states with an antisymmetric space part appears also in a single elliptic Si QD at even higher energy. Indeed, for a circular dot, there are two degenerate antisymmetric space wave functions (associated with the two angular momenta $L = \pm 1$) and thus the second higher-energy multiplet consists of 20 states. Including the 6-member lower-energy multiplet, this results in 26 SU(4) states. For an elliptic dot, the circular symmetry of the space wave functions is lifted and the multiplet of 20 states splits in two 10-state multiplets. Although overlooked, and even misinterpreted

in earlier CI calculations [31], this underlying SU(4) ⊃ SU(2) × SU(2) organization of the spectrum of a single elliptic Si quantum dot is operational in other variants of CI calculations as well, as one can attest by a careful examination of the associated CI results. Indeed in Fig. 3 of Ref. [33], panel (b) contains 16 states and panel (c) contains 10 states, for a total of 26 states.

[97] N. Rohling and G. Burkard, Universal quantum computing with spin and valley states, New Journal of Physics **14**, 083008 (2012).

[98] Ref. [30] proposes a more general framework. The case of the transition from the (1,1) to the (2,0) configuration happens by setting $N_1 = 1$ and $N_2 = 0$ in Fig. 4(b) of Ref. [30].

[99] P. Huang and X. Hu, Spin relaxation in a Si quantum dot due to spin-valley mixing, Phys. Rev. B **90**, 235315 (2014).

[100] X. Zhang, R.-Z. Hu, H.-O. Li, F.-M. Jing, Y. Zhou, R.-L. Ma, M. Ni, G. Luo, G. Cao, G.-L. Wang, X. Hu, H.-W. Jiang, G.-C. Guo, and G.-P. Guo, Giant Anisotropy of Spin Relaxation and Spin-Valley Mixing in a Silicon Quantum Dot, Phys. Rev. Lett. **124**, 257701 (2020).

[101] Z. Wang, M. Feng, S. Serrano, W. Gilbert, R. C. C. Leon, T. Tantt, P. Mai, D. Liang, J. Y. Huang, Y. Su, W. H. Lim, F. E. Hudson, C. C. Escott, A. Morello, C. H. Yang, A. S. Dzurak, A. Saraiva, and A. Laucht, Jellybean quantum dots in silicon for qubit coupling and on-chip quantum chemistry, arXiv:2208.04724.

[102] C. Yannouleas and U. Landman, unpublished.

[103] M. Abramowitz and I. A. Stegun, *Handbook of Mathematical Functions with Formulas, Graphs, and Mathematical Tables* (Dover, New York, 1964) Ch. 19.

[104] For another illustration of the adaptability of our single-particle orbital basis in the case of a symmetric double well ($\varepsilon = 0$) as the interwell distance d is varied from zero ("unified atom") to large values ("separated atoms"), see Fig. 9 in Ref. [45].